Cellular/Molecular

The Astrocytic Zinc Transporter ZIP12 Is a Synaptic Protein That Contributes to Synaptic Zinc Levels in the Mouse Auditory Cortex

Abbey Manning,[1*] Benjamin Z. Mendelson,[1*] Philip T. R. Bender,[1*] Kaitlin Bainer,[1] Rayli Ruby,[1] Victoria R. Shifflett,[1] Donald F. Dariano 3rd,[2] Bradley A. Webb,[2] Werner J. Geldenhuys,[1,3] and Charles T. Anderson[1]

Departments of [1]Neuroscience, Rockefeller Neuroscience Institute and, [2]Biochemistry and Molecular Medicine, West Virginia University School of Medicine, Morgantown, West Virginia 26506, and [3]Department of Pharmaceutical Sciences, West Virginia University School of Pharmacy, Morgantown, West Virginia 26506

Synaptically released zinc is a neuronal signaling system that arises from the actions of the presynaptic vesicular zinc transporter protein zinc transporter 3 (ZnT3). Mechanisms that regulate the actions of zinc at synapses are of great importance for many aspects of synaptic signaling in the brain. Here, we identify the astrocytic zinc transporter protein ZIP12 as a candidate mechanism that contributes to zinc clearance at cortical synapses. We identify small-molecule compounds that antagonize the function of ZIP12 in heterologous expression systems, and we use one of these compounds, ZIP12 modulator 8, to increase the concentration of ZnT3-dependent zinc at synapses in the brain of male and female mice to inhibit the activity of neuronal AMPA and NMDA glutamate receptors. These results identify a cellular mechanism and provide a pharmacological toolbox to target the molecular machinery that supports the actions of synaptic zinc in the brain.

Key words: **astrocytes; auditory cortex; Slc30a3; Slc39a12; synapses; zinc**

Significance Statement

Synaptic zinc is loaded into presynaptic glutamatergic vesicles by the protein zinc transporter 3 (ZnT3), where it is coreleased with glutamate during synaptic transmission. Evidence from clinical studies in humans shows that alterations in the expression of the neuronal zinc transporter protein ZnT3 and the astrocytic zinc transporter protein ZIP12 are associated with schizophrenia, suggesting that dysregulation of these brain-specific zinc transporter proteins may contribute altered synaptic signaling in the brain. Our results show that ZIP12 protein is expressed by astrocytes at synapses in the brain. We identify pharmacological agents that inhibit ZIP12, and we use them to modulate zinc levels in the brain. This research advances our understanding of the roles of synaptic zinc in health and disease.

Received Oct. 30, 2024; revised Dec. 10, 2024; accepted Jan. 6, 2025.

Author contributions: A.M., B.Z.M., P.T.R.B., D.F.D., B.A.W., W.J.G., and C.T.A. designed research; A.M., B.Z.M., P.T.R.B., R.R., V.R.S., K.B., D.F.D., W.J.G., and C.T.A. performed research; A.M., B.Z.M., P.T.R.B., R.R., V.R.S., K.B., D.F.D., B.A.W., W.J.G., and C.T.A. analyzed data; A.M., P.T.R.B., D.F.D., and C.T.A. wrote the paper.

We thank Hui Li for the technical assistance. We thank Dr. Kevin Daly for his comments and suggestions on the manuscript. We thank Dr. Martin Hruska for his feedback on this work. This work was supported by the Whitehall Foundation, 2020-05-44 (C.T.A); the National Institute of General Medical Sciences, R35-GM138023 (C.T.A), T32-GM132494 (A.M), T32-GM133369 (P.T.R.B), and Visual Sciences CoBRE project leader funding P20-GM144230 (B.A.W); and the National Institute on Aging, T32-AG052375 (K.B). This work was supported by West Virginia University start-up funding (C.T.A and B.A.W). This material is based upon work supported by the National Science Foundation under Grant 2326758 (C.T.A) and National Science Foundation under Cooperative Agreement No. OIA-2242771 (P.T.R.B and C.T.A). We thank the West Virginia University Microscope Imaging Facility, which has been supported by the WVU Cancer Institute and National Institutes of Health Grants P20RR016440, P30GM103488, U54GM104942, and P20GM103434.

*A.M., B.Z.M. and P.T.R.B. contributed equally to this work.

The authors declare no competing financial interests.

Correspondence should be addressed to Charles T. Anderson at charles.anderson@hsc.wvu.edu.

https://doi.org/10.1523/JNEUROSCI.2067-24.2025

Introduction

Zinc is enriched in the neocortex with ∼20% of total cortical zinc found in glutamatergic synaptic vesicles (Cole et al., 1999). This pool of zinc is termed "synaptic zinc" because it is loaded into presynaptic glutamatergic vesicles by the protein zinc transporter 3 (ZnT3) and released into the synaptic cleft along with glutamate during synaptic transmission (Cole et al., 1999; Frederickson et al., 2005; McAllister and Dyck, 2017a). There are 11 members of the zinc transporter family of proteins (ZnT, Slc30a1–11) that reduce cytoplasmic zinc by transporting it out of cells or into intracellular compartments (including synaptic vesicles) and 14 members of the Zrt, Irt-like family of proteins (ZIP, Slc39a1–14) that increase cytoplasmic zinc by transporting it into the cytoplasm from extracellular domains (ECD) and endosomal compartments (Kambe et al., 2015;

Styrpejko and Cuajungco, 2021). Different tissues have different expression levels of ZnT and ZIP proteins, and some, such as ZnT3 and ZIP12, are selectively and highly expressed in the brain (Palmiter et al., 1996; Seve et al., 2004; Chowanadisai et al., 2013) with high ZnT3 expression in a large subset of neurons (Zeisel et al., 2015; Chen et al., 2019) and high ZIP12 expression in astrocytes (Zhang et al., 2014a; Nishikawa et al., 2017; Boisvert et al., 2018), a major class of glia. Since astrocytes are an integral component of excitatory synapses (Perea et al., 2009) crucial for controlling the dynamics of glutamate reuptake after its release (Rose et al., 2018), they are well positioned to regulate other aspects of excitatory transmission, such as synaptic zinc levels.

During neurotransmission, free zinc levels in the synaptic cleft rise from nanomolar to tens of micromolar levels over millisecond timescales, returning to basal nanomolar levels within a few hundred milliseconds (Vogt et al., 2000; Vergnano et al., 2014; Morabito et al., 2022; Bender et al., 2023). This suggests the presence of a powerful system for the rapid removal of free zinc following its release, but the molecular components of this system remain unknown. ZIP12 (Slc39a12) has a very high affinity for zinc with an apparent K_m value of ~6 nM (Chowanadisai et al., 2013). Crucially, this high affinity of ZIP12 for zinc is appropriate to set the low nanomolar levels of free zinc near synaptic clefts (Vergnano et al., 2014; Anderson et al., 2015). Mounting evidence from clinical studies with humans shows that changes in the expression of ZnT3 and ZIP12 are associated with schizophrenia—a major neuropsychiatric disorder that affects ~1% of people worldwide (Insel, 2010). By analyzing postmortem brain tissue samples from people with schizophrenia compared with age-matched controls, recent studies found that schizophrenia is associated with reduced cortical *ZNT3* mRNA and protein expression (Perez-Becerril et al., 2016) and with increased *ZIP12* mRNA expression (Scarr et al., 2016; Dean et al., 2024). This indicates that ZnT3 and ZIP12 may regulate zinc signaling in people and suggests that their dysregulation may contribute to the etiology of this disorder. To date, efforts to pharmacologically affect synaptic zinc signaling using the metal chaperones clioquinol and PBT2 have had beneficial effects on the cognitive deficits observed in ZnT3 knock-out (KO) mice (Adlard et al., 2015) and aging wildtype (WT) mice (Adlard et al., 2014); however, these approaches do not exclusively affect synaptic zinc signaling, so there is a crucial need to develop more specific tools.

Here, we show that ZIP12 is expressed at cortical synapses, we identify small-molecule compounds that specifically target the function of ZIP12 in heterologous expression systems (ZIP modulators; ZiMos), and we use one of these compounds, ZIP12 modulator 8 (ZiMo12.8), to increase the inhibitory effects of synaptically released zinc on neuronal AMPA and NMDA glutamate receptors in acute brain slices of the mouse auditory cortex (ACx). Together, our results uncover mechanisms that shape synaptically released zinc and identify a pharmacological approach to target the molecular machinery important for the function of synaptic zinc at synapses in the brain.

Materials and Methods

Animal handling. WT C57Bl/6 mice (Jackson Laboratory) and ZnT3 KO mice (Jackson Laboratory) aged Postnatal Day (P)32–P35 (for histology experiments) and aged P21–P35 (for electrophysiology experiments) were used in accordance with the animal welfare guidelines and regulations of West Virginia University, the US National Institutes of Health, and the Society for Neuroscience. All procedures were approved by the Institutional Animal Care and Use Committee of West Virginia University. Both male and female mice were used in these experiments. Experiments using ZnT3 KO mice were performed blind to their genotype.

Perfusions. Male and female WT mice aged P35 were anesthetized and perfused transcardially using carbogenated artificial cerebral spinal fluid (ACSF; in mM: 130 NaCl, 3 KCl, 2.4 CaCl2, 1.3 MgCl2, 20 NaHCO3, 3 HEPES, 10 D-glucose; saturated with 95% O2/5% CO2 (vol/vol), ~300 mOsm), pH 7.25–7.35, followed by 4% paraformaldehyde (PFA) with 0.0028% glutaraldehyde in phosphate-buffered saline (PBS). Brains were immediately removed and placed into PFA overnight. Brains were then cryopreserved in 30% sucrose in PBS and sectioned coronally or sagittally at 25 µm on a microtome (Thermo Fisher Scientific Sliding Microtome Microm HM450) with a BFS-40MPA Freezing Stage (Physitemp Instruments). Sections were stored free-floating in 0.01% sodium azide in PBS at 4°C.

Immunohistochemistry. Sections were first blocked for 1 h at room temperature in blocking buffer [1% bovine serum albumin (BSA), 10% fetal bovine serum, 1% Triton X-100 in PBS]. Sections were then incubated for 48 h at 4°C with primary antibody (chicken anti-GFP, 1:1,000, Abcam, 13970; guinea pig anti-bassoon, 1:200, Synaptic Systems, 141 004; mouse IgG1 anti-ZnT3, 1:1,000, Synaptic Systems, 197 011; chicken anti-EAAT1, 1:1,000, Synaptic Systems, 250 116; mouse IgG1 anti-MAP2, 1:1,000, Synaptic Systems, 188 011; rabbit anti-ZIP12, 1:1,000, Sigma-Aldrich, AV44127) in blocking buffer and washed three times for 10 min in PBS. Sections incubated with secondary antibody (goat anti-chicken Alexa Fluor 488, Jackson ImmunoResearch Laboratories, 103-545-1555; goat anti-guinea pig Alexa Fluor 555, Invitrogen, A-21435; goat anti-mouse IgG1 Alexa Fluor 555, Invitrogen, A-21127; goat anti-rabbit Alexa Fluor 594, Jackson ImmunoResearch Laboratories, 111-585-144; goat anti-mouse IgG1 Alexa Fluor 594, Jackson ImmunoResearch Laboratories, 115-587-158; goat anti-rabbit Alexa Fluor Plus 647, Invitrogen, A32733TR; goat anti-rabbit Alexa Fluor 750, Invitrogen, A-21039) in blocking buffer (1:500) for 2 h at room temperature, washed three times in PBS for 10 min, washed two times in 0.1 M phosphate buffer for 5 min, and mounted to glass slides with ProLong Glass Antifade Mountant (Invitrogen) and covered with a No.1.5 glass coverslip.

Fluorescent imaging and analysis. The 20 × 20 µm (1,024 × 1,024 pixel) confocal *Z*-stacks (0.2 µm *Z*-step) were obtained using Leica Stellaris 8 with a 100× oil immersion objective. *Z*-stacks were analyzed using Fiji (Schindelin et al., 2012). A Gaussian blur (sigma of 0.04 µm) was applied to each image to filter out noise. To determine puncta distance and puncta overlap, images were analyzed through the Fiji plugin DiAna. Puncta were determined with an XY radius of 3.0 (0.06 µm) and *Z* radius of 2.0 (0.04 µm) and noise of 15.0. Thresholding was set to the mean fluorescence intensity of the *Z*-stack + 2 × standard deviation of the mean fluorescence intensity and a minimum volume of 15 pixels. Puncta overlap was calculated as the percentage of each EAAT1 (Fig. 1*C*) or ZIP12 (Fig. 1*E*) punctum volume that overlapped with a bassoon, ZnT3, or ZIP12 punctum. Pairs of puncta with zero percentage overlap are excluded from these calculations. To determine the dendritic spine size, fluorescent images of GFP-expressing dendrites were obtained, and the head of each spine within each image was selected and thresholded. The area of each spine head was determined automatically using Fiji's measurement tool. The presence of a protein at each synapse was determined through a statistical measure of puncta fluorescence against the background fluorescence of a 1 × 1 µm area around the puncta. Expression was defined as the mean puncta fluorescence intensity being greater than the mean + 2× standard deviation of the mean background fluorescence intensity. Fluorescence intensity was determined automatically using Fiji's measurement tool. Rotation analysis was performed by rotating one of the fluorescent channels in multicolor images 90° clockwise as indicated in the corresponding figure legend. This analysis can reveal spatial association between puncta if image rotation reduces the number of spatially overlapping pairs of puncta and the percentage of overlapping pixels shared by overlapping puncta; the

number of pairs of puncta resulting from rotation analysis is listed in the corresponding figure legend.

HEK293 compound screening. HEK293 cells (ATCC) were transfected with 0.67 mg of human Myc-DDK-ZIP12 cDNA (OriGene plasmid, RC227331) using FuGene HD (Qiagen). ZIP12 cDNA-transfected HEK293 cells were then placed in 60 wells of a 98-well plate. Cell culture media were vacuumed from wells and 60 µl of a 1 µM FluoZin-3, AM and 1 µM CellTracker Red CMPTX (Thermo Fisher Scientific) in clear serum-free media were added to each well. The cells were incubated for 30 min at 37°C. After incubation, the media were removed and replaced with clear HBSS. The wells were then rinsed, and each well was given either one compound (1 µM per well, 50 wells) or a dimethyl sulfoxide (DMSO) vehicle (10 wells). The well plate was immediately taken to a plate reader for fluorescent zinc uptake assay. The assay consisted of 300 s of a baseline measurement of FluoZin-3 fluorescence intensity without any $ZnCl_2$ and then 300 s of measuring fluorescence intensity after the addition of 0.5 µM $ZnCl_2$. The zinc-insensitive CellTracker Red CMPTX fluorescence was also measured throughout the assay as a control and used as a normalization for FluoZin-3 cell fluorescence. To normalize fluorescence data, a ratio was calculated by dividing the FluoZin-3 fluorescence intensity measurements by the CellTracker Red CMPTX fluorescence intensity measurements within the same well. This normalization accounted for variation in cell number between wells. The change in fluorescence from the baseline to the addition of $ZnCl_2$ was then calculated for each compound and compared with the vehicle (Fig. 3*D*). The difference to the vehicle for each compound was then graphed and compared with every other compound, where a negative difference indicated an antagonist (Fig. 3*E*). For experiments shown in Figure 3, *J* and *K*, the high-affinity, fast, cell-permeant zinc chelator TPA (20 µM; Huang et al., 2013) was added to the bath to reduce the zinc-dependent fluorescence of FluoZin-3 and verify that the fluorescence increases following $ZnCl_2$ addition were not due to non zinc-dependent sources such as autofluorescence signals that can increase over time due to metabolic stress (Surre et al., 2018) or due to phototoxicity from the excitation light used in fluorescent imaging (Icha et al., 2017).

Virtual compound screening. The virtual screen was performed by docking Hit2Lead (ChemBridge) compounds into putative binding pockets of the ZIP12-ECD. The structure of ZIP12 was obtained from AlphaFold v4 (AF-Q5FWH7-F1-v4) and the dimerization interface identified by a structural and sequence alignment of this model with the ZIP4-ECD monomer (PDBID:4XA2). From our Hit2Lead compound list, we generated 3-D .sdf files of each compound by conversion of their SMILES to 2-D representations, and then 3-D representations using the MMF94 + s forcefield in RDKit (rdkit.org). The subregion of the ZIP12 model was selected, and each ligand was virtually docked within the AutoDock Vina Extension available in the SAMSON software suite (Trott and Olson, 2010; Eberhardt et al., 2021). Using the DataWarrior structural–activity relationship (SAR) suite (openmolecules.org), analysis was performed by combining data from both previously screened and unscreened compounds to determine substructure similarities that consistently resulted in high inhibition of "in cell" tests (Sander et al., 2015).

Western blot. Cell culture samples were obtained by first rinsing cells within the six-well plate with cold PBS and then vacuumed. More PBS was added, and a cell scraper was used to free cells from the bottom of the well plate to be pipetted into microcentrifuge tubes. The cells were centrifuged for 5 min at 1,500 RPM, and the supernatant was discarded. Samples were then incubated with RIPA buffer (Sigma-Aldrich) and a protease inhibitor cocktail (1 mM AEBSF, 800 nM aprotinin, 50 µM bestatin, 15 $\mu M \times 10^{-64}$, 20 µM leupeptin, 10 µM pepstatin A, 5 mM EDTA; Thermo Fisher Scientific) on ice for 30 min, centrifuged for 10 min at 12,000 RPM and 4°C, and the supernatant was saved. Using the Pierce BCA Protein Assay Kit (Thermo Fisher Scientific), the concentration of each sample was determined, and sample concentrations were then reduced to the lowest sample concentration using Milli-Q ultrapure water. Samples were then mixed 1:1 with 5% β-mercaptoethanol (Thermo Fisher Scientific) in 2× Laemmli sample buffer (Bio-Rad Laboratories) and boiled for 5 min at 100°C. Samples were separated on 4–20% Mini-PROTEAN TGX Gels (Bio-Rad Laboratories) and transferred to 0.2 µm PVDF membrane (Bio-Rad Laboratories) using a 25 mM Tris, 192 mM glycine, 0.1% (*w*/*v*) SDS buffer (Bio-Rad Laboratories). The membrane was first blocked using 3% BSA (G-Biosciences) for 1 h at room temperature and then incubated with rabbit anti-ZIP12 primary antibody in 3% BSA (1:1,000, Sigma-Aldrich, AV44127) overnight at 4°C. The membrane was washed three times in PBS (Fisher Bioreagents) with 0.1% Tween 20 (T, Sigma-Aldrich) for 15 min. The membrane was then incubated with goat anti-rabbit secondary antibody conjugated to horse radish peroxidase (1:2,000, Bio-Rad Laboratories, 1721019) in PBST for 1 h at room temperature and washed three times for 15 min with PSBT. SuperSignal West Pico PLUS Stable Peroxide (Thermo Fisher Scientific) was mixed 1:1 with SuperSignal West Pico PLUS Luminol/Enhancer (Thermo Fisher Scientific) and placed gently over the membrane and imaged using an Amersham Imager 680 (GE Life Sciences). After imaging, the membrane was rinsed with PBST, incubated with rabbit anti-glyceraldehyde 3-phosphate dehydrogenase (GAPDH; 1:1,000, Bio-Rad Laboratories, VPA00187) in 3% BSA overnight at 4°C, and then washed three times with PBST for 15 min. The membrane was incubated with goat anti-rabbit secondary antibody conjugated to horse radish peroxidase (1:2,000, Bio-Rad Laboratories, 1721019) in PBST for 1 h at room temperature, washed three times for 15 min with PSBT, and then imaged as previously described. To quantify the bands, the Western blots were analyzed using Fiji (Schindelin et al., 2012). The intensity of each band was measured through Fiji's automatic measuring tool. The background surrounding each band was measured the same way and subtracted from the band intensity. The resulting band intensities were then made into a ratio of ZIP12 band intensity/GAPDH band intensity.

Stereotaxic surgeries. Male and female WT and ZnT3 KO mice at P21–P28 were anesthetized with inhaled isoflurane (induction, 3% in oxygen; maintenance, 1.5% in oxygen) and secured in a stereotaxic frame (Stoelting). Core body temperature was maintained at ~37°C with a heating pad, and eyes were protected with ophthalmic ointment. Lidocaine (1%) was injected under the scalp, and an incision was made into the skin at the midline to expose the skull. Using a 27 gauge needle as a scalpel, a small craniotomy (~0.4 mm diameter) was made over the inferior colliculus at coordinates 1.3 mm posterior and 1.0 mm lateral to the lambda. Borosilicate glass pipettes (VWR International) were pulled to a shallow taper (length, >1 cm; tip diameter, ~30 µm) and advanced into the region of interest at an angle ~25° off the horizontal plane. Injection pipettes were backfilled with mineral oil (Sigma-Aldrich) and filled with pGP-AAV-syn-jGCaMP8m-WPRE (titer 5e12–5e13 genome copies/mL, Addgene) or cholera toxin subunit B conjugated to Alexa Fluor 555 (CTB-555, 1 mg/µl, Thermo Fisher Scientific). They were connected to 5 µl glass syringes (Hamilton) via capillary tubing and controlled with syringe pumps (World Precision Instruments). Pipettes were inserted 1.5 mm deep into the craniotomy, and 0.4 µl of CTB-555 was injected at 0.2 µl per minute for 2 min, or 0.9 µl of AAV was injected at 0.3 µl per minute for 3 min. After injections, the pipettes were left in place for 2 min prior to removal, and then the scalp of the mouse was closed with cyanoacrylate adhesive. Mice received an injection of nonsteroidal anti-inflammatory drug meloxicam during the injection procedure and a diet of meloxicam tablets (Bio-Serv) for 72 h after surgery. Mice were monitored for signs of postoperative stress and pain.

Brain slice electrophysiology. Acute brain slice experiments using WT and ZnT3 KO (P25–P35) male and female mice were performed as previously described (Bender et al., 2023). Slices were examined during experiments to confirm accurate placement of the injection sites. Brain slices of ACx were cut in chilled carbogenated choline-based solution of the following composition (in mM): 110 choline chloride, 25 $NaHCO_3$, 25 D-glucose, 11.6 sodium ascorbate, 3.1 sodium pyruvate, 2.5 KCl, 0.5 $CaCl_2$, 7 $MgCl_2$. AMPA receptor miniature excitatory

postsynaptic current (mEPSC) experiments were carried out using carbogenated ACSF with the following composition (in mM): 130 NaCl, 3 KCl, 2.4 $CaCl_2$, 1.3 $MgCl_2$, 20 $NaHCO_3$, 3 HEPES, 10 D-glucose, 0.0005 tetrodotoxin (TTX), saturated with 95% O_2/5% CO_2 (vol/vol), pH 7.25–7.35, ~300 mOsm. All solutions were continuously bubbled with carbogen. Contaminating zinc was removed from the ACSF for all experiments by stirring the ACSF with Chelex 100 resin (Bio-Rad Laboratories) for 1 h. High-purity $CaCl_2$ and $MgCl_2$ salts (99.995% purity; Sigma-Aldrich) were added to the ACSF after the Chelex resin was filtered using Nalgene rapid flow filters lined with polyethersulfone (0.2 µM pore size). All plastic and glassware were washed with 5% high-purity nitric acid. Mice were first anesthetized with isoflurane and then immediately decapitated. Brains were rapidly removed, and coronal slices (300 µm) of the cortex were prepared in chilled choline chloride cutting solution using a vibratome (VT1200 S; Leica Biosystems). Slices were then transferred into a holding chamber of carbogenated ACSF and incubated for ~30 min at 35°C and then incubated at room temperature for ~30 min before electrophysiological experiments were performed. For electrophysiological experiments, slices were transferred into the recording chamber and perfused with carbogenated ACSF at a rate of 1–2 ml/min. Recordings were performed at 30–32°C using an in-line heating system (Warner Instruments). Corticocollicular neurons were identified by their labeling with the retrograde labeler cholera toxin subunit B conjugated to Alexa Fluor 555 (Thermo Fisher Scientific). Electrophysiological recordings were made using an amplifier (MultiClamp-700B, Axon Instruments), a digital to analog converter (USB-6229, National Instruments), and ephus (Suter et al., 2010). Voltage-clamp recordings were conducted using borosilicate pipettes (Warner Instruments) pulled to tip resistances of 3–5 MΩ (Sutter Instrument) filled with a cesium-based internal solution with the following composition (in mM): 128 cesium-methanosulfonate, 10 HEPES, 4 $MgCl_2$, 4 Na, 2 ATP, 0.3 Tris-GTP, 10 Tris-phosphocreatine, 0.5 cesium-EGTA, 3 Na-ascorbate, 1 QX314, pH 7.23 (303 mOsm) at −70 mV holding. Series (R_{series}) and input resistance (R_{input}) were determined in a voltage-clamp mode (command potential set at −70 mV) by giving a −5 mV voltage step, which resulted in transient current responses. R_{series} was determined by dividing the −5 mV voltage step by the peak current value generated immediately after the step in the command potential. The difference between the baseline and steady-state hyperpolarized current (ΔI) was used to calculate R_{input} using the following formula: $R_{input} = -5\ mV/\Delta I - R_{series}$. Membrane time constant (τ; in msec) is the weighted time constant calculated via fitting a double exponential to the decay phase of the test step. Cell capacitance (in picofarads) was calculated by dividing the time constant by the input resistance. Current density was calculated as the holding current divided by the capacitance of the cell. For tonic NMDA receptor current experiments, a modified low-magnesium ACSF was used, with the following composition (in mM): 130 NaCl, 3 KCl, 2.4 $CaCl_2$, 0.05 $MgCl_2$, 20 $NaHCO_3$, 3 HEPES, 10 D-glucose, 0.0005 TTX, 0.02 SR95531 (gabazine), 0.025 DNQX, and 0.01 glycine, saturated with 95% O_2/5% CO_2 (vol/vol), pH 7.25–7.35, ~300 mOsm. AP5 (50 µM), ZX1 (300 µM), ZiMo12.8 (10 µM), and ZiMo12.9 (10 µM) were bath applied where indicated. ZiMo12.8 and ZiMo12.9 were dissolved in DMSO.

Statistical analysis. Analysis was performed with Fiji (Schindelin et al., 2012), MATLAB (MathWorks), and Prism (GraphPad). For statistical comparisons, a Student unpaired *t* test was used if the group data passed Lilliefors test for normality. If the group data were not normally distributed, a Kruskal–Wallis one-way ANOVA was used. A statistical comparison was determined to be significant if the *p* value was <0.05 for single comparisons or by use of Dunn's multiple-comparison test for multiple comparisons. Statistically significant differences are denoted in figures with an asterisk (*), and *p* values are listed in the figure legends. Statistical analyses were performed using Prism (GraphPad), MATLAB (MathWorks), and Excel (Microsoft). Bar plots show the mean with error bars representing ±standard error of the mean (SEM). Detailed information about the statistical tests used are available in Extended Data Table 1-1.

Results

To investigate the potential roles of ZIP12 in synaptic function, we first assessed the expression pattern of ZIP12 protein in the brain. Single-cell sequencing studies have consistently found that ZIP12 mRNA expression is highly enriched in astrocytes compared with other types of brain cells (Fig. 1*A*; Zhang et al., 2014b; Zeisel et al., 2015; Clarke et al., 2018; Yao et al., 2021). Since ZIP12 is a zinc transporter protein that targets the plasma membrane (Chowanadisai et al., 2013), we hypothesized that ZIP12 protein would be expressed by astrocytes in the brain and would be localized to synapses. To address these hypotheses, we performed immunohistochemical staining for ZIP12 in brain sections of mouse ACx (see Materials and Methods; Fig. 1*B*). Along with ZIP12, we also stained for the synaptic proteins bassoon (a presynaptic protein that assists in tethering vesicles at the active zone of synapses; Takao-Rikitsu et al., 2004; tom Dieck et al., 2005; Magupalli et al., 2008) and excitatory amino acid transporter 1 (EAAT1; an astrocytic protein that is responsible for glutamate reuptake into astrocytes after it is released from presynaptic terminals; Bunch et al., 2009; Fig. 1*B*). We hypothesized that if EAAT1, bassoon, and ZIP12 are also closely associated, this would support the role of astrocytic ZIP12 expression at synapses. We quantified these relationships and found that, consistent with our hypothesis, EAAT1 was closely associated with ZIP12 and bassoon (Fig. 1*C*), suggesting that EAAT1 and ZIP12 are proteins expressed in astrocytic processes near the active zone of synapses (Takao-Rikitsu et al., 2004; tom Dieck et al., 2005; Magupalli et al., 2008). Next, we hypothesized that if astrocytic ZIP12 interacts with synaptically released zinc at synapses, ZIP12 and ZnT3 would also show a high degree of colocalization. To test this hypothesis, we performed staining for ZnT3, ZIP12, and bassoon as above. We found a significant association of ZIP12 with ZnT3 with bassoon (Fig. 1*D*,*E*) in the cortex, suggesting that ZIP12 and ZnT3 might function to support synaptic zinc release and clearance. Together, these results suggest that astrocytes express the transporter proteins ZIP12 and EAAT1 which interact with zinc and glutamate in synaptic terminals after they are released from presynaptic vesicles during synaptic transmission.

Given the association between ZnT3 and ZIP12 puncta in the brain, we hypothesized that these proteins would localize to postsynaptic structures. To address this, we performed stereotaxic injections of a retrograde AAV-GCaMP8m (see Materials and Methods) into the right inferior colliculus of WT mice to induce the expression of GCaMP8m in Layer 5 corticocollicular neurons in the ACx (Fig. 2*A*). We stained mouse cortical sections for MAP2 and ZIP12 to orient ZIP12 to the dendritic organization of GFP-expressing neurons in the cortex (Fig. 2*A*). We next quantified the relationship of ZIP12 and ZnT3 with postsynaptic dendritic spines in the cortex with antibodies for ZIP12 and ZnT3 (see Materials and Methods). Using GFP fluorescence, dendritic spines in layer 2/3 of the cortex were imaged and analyzed using a threshold measure of the spine head area (Fig. 2*B*–*F*; Hruska et al., 2022; Manning et al., 2024). Consistent with the association of ZnT3 with larger dendritic spines in the cortex (Manning et al., 2024), ZIP12 was also expressed at larger dendritic spines (Fig. 2*F*), with a majority of dendritic spines located at synapses that coexpress astrocytic ZIP12 and neuronal ZnT3 (Fig. 2*G*,*H*). Together, these results show that presynaptic ZnT3 and astrocytic ZIP12 are both associated with postsynaptic dendritic spines in the cortex, suggesting that these proteins are functionally coordinated with each other at synapses.

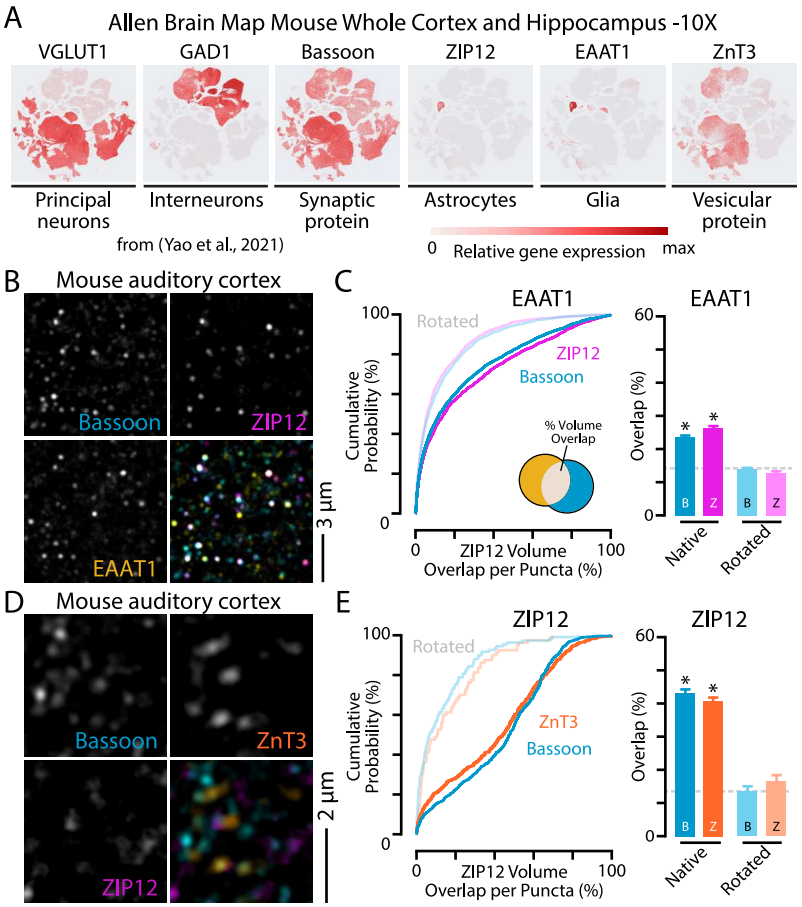

Figure 1. ZIP12 is a synaptic protein. ***A***, Relative gene expression of ZIP12 showing high expression in astrocytes. Also shown are markers for glia (EAAT1), neurons (GAD1, VGLUT1, and bassoon), and vesicles (ZnT3). Images are scatterplot projections of single-cell RNA sequencing data generated from data in Yao et al. (2021), accessed at celltypes.brain-map.org/rnaseq and celltypes.brain-map.org/rnaseq/mouse_ctx-hpf_10x, and displayed in accordance with Allen Institute Transcriptomics Explorer citation policy. ***B***, Example image of bassoon (cyan), ZIP12 (magenta), and EAAT1 (yellow) puncta in Layer 2/3 of mouse ACx. ***C***, Left, Cumulative distribution of the overlap between EAAT1 and bassoon (cyan) puncta and EAAT1 and ZIP12 (magenta) puncta. The cartoon inset shows the volume measured was where the EAAT1 punctum (yellow) and either a ZIP12 (magenta) or bassoon (cyan) punctum overlapped. Right, Average volume overlap for all pairs of puncta natively and with the EAAT1 channel rotated (bassoon, $p < 1.00 \times 10^{-15}$; native, 3,804 pairs; rotated, 2,973 pairs; ZIP12, $p < 1.00 \times 10^{-15}$; native, 1,889 pairs; rotated, 1,309 pairs; $n = 3$ mice; Kruskal–Wallis test with Dunn's multiple comparisons). ***D***, Example image of bassoon (cyan), ZnT3 (orange), and ZIP12 (magenta) puncta in layer 2/3 of mouse ACx. ***E***, Left, Cumulative distribution of the overlap between ZIP12 and bassoon (cyan) puncta and ZIP12 and ZnT3 (orange) puncta. Right, Average volume overlap for both pairs of puncta natively and with the ZIP12 channel rotated (bassoon, $p = 1.92 \times 10^{-13}$; native, 519 pairs, rotated, 109 pairs; ZnT3, $p < 1.00 \times 10^{-15}$; native, 711 pairs; rotated, 80 pairs; $n = 3$ mice; Kruskal–Wallis test with Dunn's multiple comparisons). Asterisks (*) indicate statistically significant values. All values are given as mean ± SEM.

Having established that ZIP12 is expressed at synapses in the mouse cortex, we next sought methods to assess the functional consequences of ZIP12 on synaptic signaling. Specifically, we were interested in a method to reduce ZIP12 function because this could have therapeutic applications in disease models related to upregulation of ZIP12 expression, such as schizophrenia (Scarr et al., 2016; Dean et al., 2024). As a first step toward this goal, we established a ZIP12 activity assay based on heterologous expression systems that have been previously used to study the function of zinc transporters such as ZIP4 (Zhang et al., 2016, 2017; Hoch et al., 2020), ZIP13 (Bin et al., 2011), and ZnT5 (Ohana et al., 2009). HEK293 cells were transfected with human Myc-tagged ZIP12 cDNA, and zinc uptake was determined using a fluorescent indicator in both transfected and native cells (Hoch et al., 2020). Transfection with ZIP12 cDNA resulted in increased ZIP12 expression by HEK293 cells (Fig. 3*A*). We quantified zinc uptake in HEK293 cells with FluoZin-3, AM—an intracellular, Zn^{2+}-selective indicator that increases in fluorescence when bound to zinc (Hoch et al., 2020). 0.5 µM $ZnCl_2$ was added to both native and ZIP12-transfected HEK293 cells (Fig. 3*B*). Consistent with expression of ZIP12 resulting in increased zinc transport into HEK293 cells, zinc application to cells transfected with ZIP12 cDNA resulted in increased fluorescent intensity compared with native cells (Fig. 3*C*). Having established a ZIP12 transport assay, we screened 610 compounds (1 µM) from a small-molecule library (Hit2Lead, ChemBridge; Fig. 3*D*,*E*) on ZIP12-transfected HEK293 cells. We quantified the effects of these putative ZIP12 modulator (ZiMo12) compounds on ZIP12 function by normalizing the changes in FluoZin-3 fluorescence compared with vehicle in ZIP12-transfected HEK293 cells and ranked the effect of the compounds from most antagonistic to most agonistic (Fig. 3*E*). Next, we sought to identify structural similarities between antagonist compounds by performing a virtual docking experiment combined with SAR analysis. Virtual docking experiments were performed by docking compounds into a putative binding site on the ZIP12 dimerization interface (see Materials and Methods; Fig. 3*F*,*G*,*H*; Extended Data Table 2-1). We focused on this dimerization interface because these residues are crucial for the homodimerization and zinc transport capacity of ZIP4,

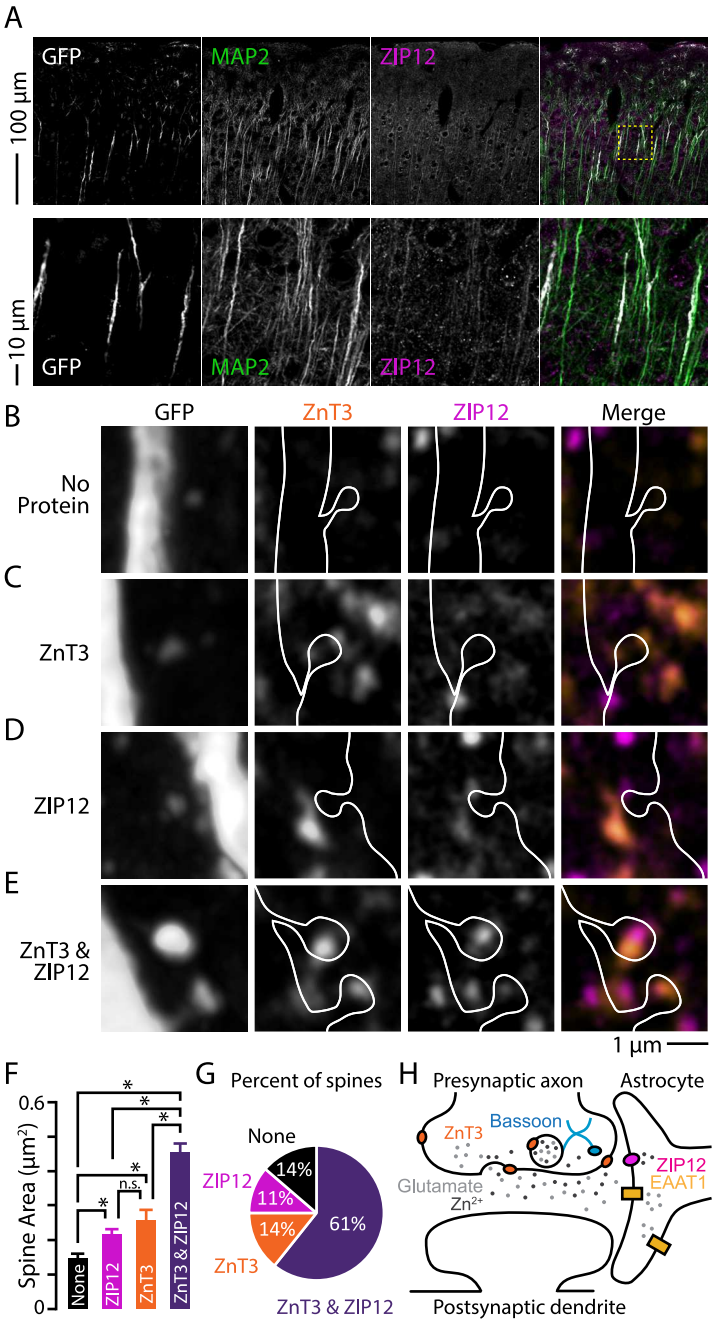

Figure 2. ZIP12 and ZnT3 are associated with dendritic spines. ***A***, Top, Example image of corticocollicular neurons (GFP; white), MAP2 (green), and ZIP12 (magenta) in the ACx. Yellow dotted box indicates area imaged for bottom. Bottom, Zoomed in example of corticocollicular neurons and spines (GFP; white), MAP2 (green), and ZIP12 (magenta) in layer 2/3 of the ACx. ***B***, Example image of a synapse in layer 2/3 that does not express any zinc transporter proteins. White outline indicates the dendrite and dendritic spine. Merged image shows ZnT3 (orange) and ZIP12 (magenta) stains. ***C***, Example image of a synapse that only expresses ZnT3. Same color scheme as in ***B***. ***D***, Example image of a synapse that only expresses ZIP12. Same color scheme as in ***B***. ***E***, Example image of a synapse that expresses both ZnT3 and ZIP12. Same color scheme as in ***B***. ***F***, Average spine areas for synapses with no zinc transporters (black), just ZIP12 (magenta), just ZnT3 (orange), and both zinc transporters (purple) (none $n = 23$ spines; ZIP12 $n = 19$ spines; ZnT3 $n = 24$ spines; ZnT3 and ZIP12 $n = 103$ spines in three mice; none-ZIP12, $p = 3.43 \times 10^{-3}$; none-ZnT3, $p = 2.50 \times 10^{-3}$; none-ZnT3 and ZIP12, $p = 7.00 \times 10^{-8}$; ZIP12-ZnT3, $p = 0.2746$; ZIP12-ZnT3 and ZIP12, $p = 9.17 \times 10^{-5}$; ZnT3-ZnT3 and ZIP12, $p = 3.94 \times 10^{-4}$; unpaired *t* test). ***G***, Pie chart showing the percentage of total synapses with no zinc transporters, just ZIP12, just ZnT3, and both zinc transporters. Same color scheme as ***G***. ***H***, Cartoon showing the tripartite synapses based on the results in ***A–G***. Asterisks (*) indicate statistically significant values. All values are given as mean ± SEM.

another member of the LIV-I family of zinc transporter proteins and close homolog to ZIP12 (Kambe et al., 2015; Zhang et al., 2016, 2017). The dimerization interface was targeted by homology modeling in which the sequence of ZIP12 was mapped onto the structure of ZIP4 (Fig. 3*F*,*G*). Our results showed that compounds with the highest inhibition and highest predicted binding affinity were consistently bound to the linker region connecting the ECD of ZIP12. These compounds all contained four cyclic rings which were generally nonpolar while also having relatively high flexibility owing to separation of cyclic structures.

Based on these results, four compounds with high predicted binding affinity to ZIP12 and that experimentally acted as antagonists were used in further trials to assess ZIP12 specificity (Fig. 3*I*,*J*). To assess specificity of these compounds on ZIP12 versus other proteins expressed by HEK293 cells, we performed

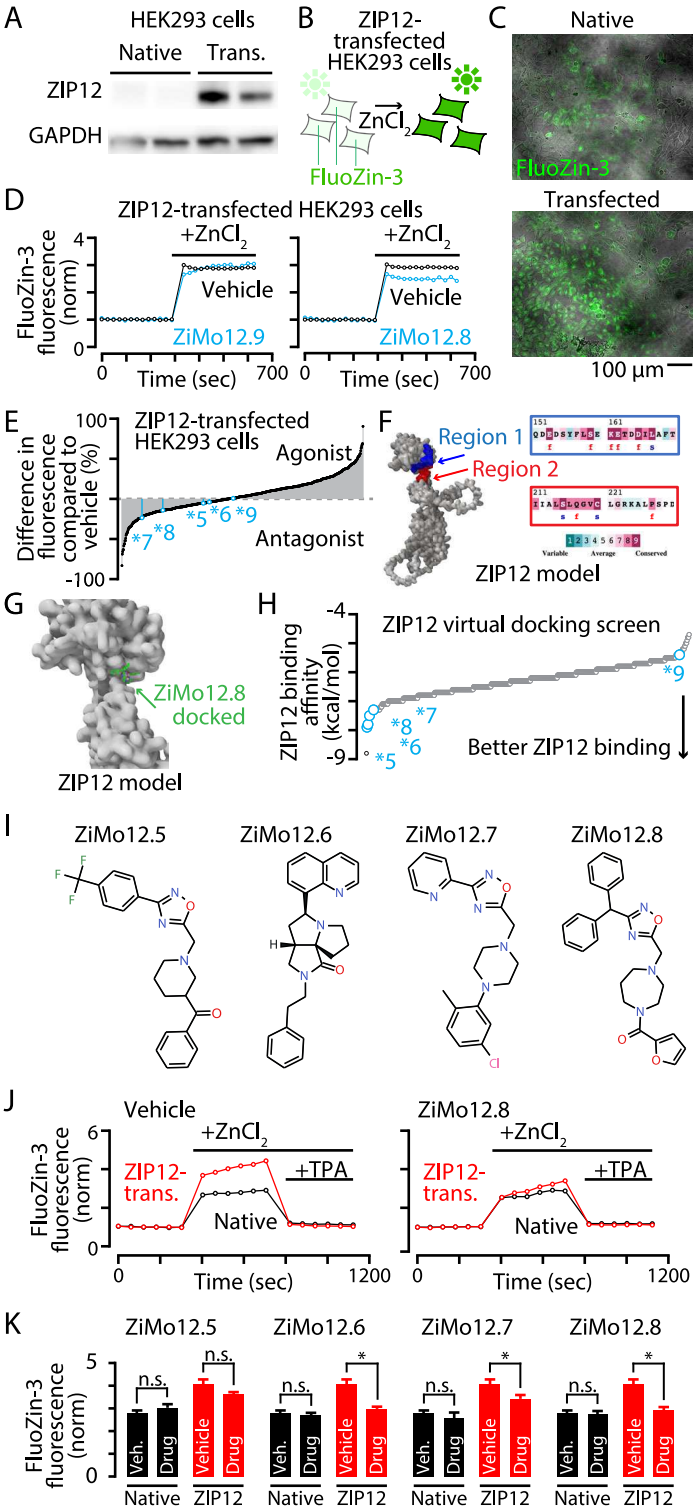

Figure 3. Identifying small-molecule compounds that reduce ZIP12-mediated zinc fluorescence in HEK293 cells. ***A***, Top, Western blot bands for ZIP12 (top) and GAPDH (bottom) from native and ZIP12 cDNA-transfected HEK293 cells. ***B***, Cartoon depicting the function of FluoZin-3. With the addition of $ZnCl_2$, the cells will fluoresce more. ***C***, Example images of native (top) and transfected (bottom) HEK293 cells with FluoZin-3 after the addition of $ZnCl_2$. ***D***, Example high-throughput zinc uptake assay traces in transfected HEK293 cells with either a vehicle (black) or a test compound (cyan). Examples show a compound with no effect on FluoZin-3 fluorescence (ZiMo12.9) and a compound that reduced FluoZin-3 fluorescence (ZiMo12.8). ***E***, The difference in fluorescence for each test compound compared with the vehicle after the addition of $ZnCl_2$. Cyan labels indicate key compounds. ***F***, Left, Space-filling model of ZIP12 (AF-Q504Y0-F1-v4) Regions 1 and 2 colored blue and red, respectively. Right, Conservation scores of residues located within Region 1 and Region 2 (arbitrary designation) of a putative binding pocket of ZIP12. ConSurf (Ashkenazy et al., 2016; Yariv et al., 2023) run of 150 ZIP12 homologs shows that both regions contain clusters of structurally (s) and functionally (f) conserved residues. ***G***, Docked pose of ZiMo12.8 (stick diagram) in pocket of ZIP12 shown as a space-filling model (gray). ***H***, The binding affinity to the ECD of ZIP12 for each compound tested. Cyan labels indicate key compounds. ***I***, The molecular structure for the four compounds chosen for further experiments. ***J***, Example zinc uptake assay traces of native (black) and ZIP12-transfected (red) HEK293 cells with the prior addition of a vehicle (left) or a compound (right). ***K***, The average fluorescence of FluoZin-3 after the addition of $ZnCl_2$ in native (black) and ZIP12-transfected (red) HEK293 cells. The left bar indicates the addition of a vehicle while the right is the addition of a compound (native vehicle $n = 6$ wells; ZIP12 vehicle $n = 6$ wells; ZiMo12.6 vs ZIP12; $p = 8.9 \times 10^{-4}$; ZiMo12.7 vs ZIP12; $p = 0.0393$; ZiMo12.8 vs ZIP12; $p = 0.0010$; $n = 6$ wells per group; unpaired t test). Asterisks (*) indicate statistically significant values. All values are given as mean ± SEM.

additional experiments comparing the effects of these compounds in native HEK293 cells versus ZIP12-transfected HEK293 cells. With these additional trials, the membrane-permeable zinc chelator TPA was added at the end of the imaging session to return the fluorescence back to the baseline, ensuring that the fluorescence signals were zinc-dependent. Both transfected and native HEK293 cells underwent the zinc uptake assay in the presence of either vehicle or one of the top compounds (Fig. 3*J*). Three of these four compounds were able to reduce the zinc-mediated increase in FluoZin-3 fluorescence of ZIP12-transfected HEK293 cells to levels similar to untransfected HEK293 cells, suggesting that they are specifically acting to reduce the zinc transport capacity of ZIP12 expressed by transfected HEK293 cells (Fig. 3*K*). Together, these results suggest that the effects of these compounds on FluoZin-3 fluorescence are ZIP12 expression-dependent and are not due to other mechanisms—such as directly chelating zinc or directly affecting FluoZin-3 fluorescence—in this screening assay.

Having identified putative ZIP12 antagonists using SAR analysis combined with heterologous expression systems, we next set out to assess the effect of ZIP12 antagonist compounds on synaptic function. Because ZiMo12.8 had the largest effect on FluoZin-3 fluorescence in ZIP12-expressing HEK293 cells (28% signal reduction; Fig. 3*K*) and had the smallest effect on native HEK293 cells (1% signal reduction; Fig. 3*K*), we focused on this compound for experiments in acute brain slices of mouse ACx. We hypothesized that if ZIP12 contributes to synaptic zinc clearance following its release into the synaptic cleft, ZiMo12.8 could increase zinc levels by reducing the zinc transport capacity of ZIP12 (Fig. 4*A*) and thereby increase zinc inhibition of glutamate receptors (McAllister and Dyck, 2017b). To test this hypothesis, we labeled layer 5 corticocollicular neurons by performing a stereotaxic injection of retrograde axonal tracer cholera toxin subunit B conjugated to Alexa Fluor 555 (CTB-555) into the right inferior colliculus of mice (Fig. 4*B*,*C*). We then prepared acute brain slices containing the ACx and visually targeted fluorescent neurons for electrophysiological recordings. Whole-cell patch–clamp recordings were performed under voltage-clamp conditions in the presence of TTX to block sodium channels and isolate action potential-independent AMPA receptor-mediated miniature excitatory postsynaptic currents (mEPSCs; Fig. 4*D*). The addition of ZiMo12.8 resulted in a significant decrease in AMPA receptor mEPSC amplitudes, consistent with increased zinc levels in the cleft that became inhibitory to AMPA receptors (Blakemore and Trombley, 2004, 2019) by reducing the zinc transport activity of ZIP12 (Fig. 4*E*–*G*). The effects of ZiMo12.8 were dependent on the presence of synaptic zinc, because similar experiments using ZiMo12.8 in ZnT3 KO mice—which lack synaptic zinc—resulted in no changes to AMPA receptor mEPSC amplitudes (Fig. 4*H*–*J*). Furthermore, in WT mice, the high-affinity, extracellular, zinc-specific chelator ZX1 (Pan et al., 2011; Anderson et al., 2015; Kalappa et al., 2015; Morabito et al., 2022; Upmanyu et al., 2022; Bender et al., 2023) occluded the effects of ZiMo12.8 on mEPSC amplitudes. Together, these results suggest that the effects of ZiMo12.8 on AMPA receptor mEPSCs are due to increasing extracellular ZnT3-dependent zinc levels (Fig. 4*K*–*M*), that these effects can be occluded by genetic or pharmacological removal of zinc from synapses, and that ZiMo12.8 does not act directly on AMPA receptors in the absence of zinc.

These electrophysiological results are consistent with ZiMo12.8 causing a ZnT3-dependent, ZX1-sensitive increase in extracellular zinc levels at synaptic connections in the brain. However, because changing zinc levels can have a range of effects on AMPA receptor function (from enhancement, to suppression, to no effect; Blakemore and Trombley, 2004; Pan et al., 2011; Kalappa et al., 2015; Blakemore and Trombley, 2019; Bender et al., 2023), we hypothesized that the summation of these different effects of zinc on AMPA receptor function combine into the small but significant decrease in mEPSC amplitudes by ZiMo12.8. Although these results are consistent with an increase in synaptic zinc levels by ZiMo12.8, the range of possible effects of increasing zinc levels on AMPA receptor function is a potential caveat to this interpretation. To address this, we utilized a complimentary approach to assess the effects of ZiMo12.8 on zinc levels in the brain. Because NMDA receptors are unidirectionally inhibited by increased zinc levels (Paoletti et al., 1997; Rachline et al., 2005; Tovar and Westbrook, 2012; Hansen et al., 2014), we hypothesized that if the inhibition of AMPA receptor function we observe is due to ZiMo12.8 increasing zinc levels, this increase in zinc should also cause inhibition of NMDA receptor function. To test this hypothesis, we performed whole-cell patch–clamp recordings under voltage-clamp conditions in ACSF containing low levels of magnesium to remove the NMDA pore block by magnesium at negative membrane potentials (Mayer et al., 1984; Bender et al., 2023). The ACSF also contained TTX, SR95531 (gabazine), the AMPA receptor antagonist DNQX, and the NMDA receptor agonist glycine in order to isolate NMDA receptor-mediated tonic currents (Povysheva and Johnson, 2012). The addition of ZiMo12.8 decreased the tonic currents (Fig. 5*A*–*E*), consistent with ZiMo12.8 increasing zinc inhibition of NMDA receptors (Paoletti et al., 1997; Rachline et al., 2005; Tovar and Westbrook, 2012; Hansen et al., 2014). AP5 further reduced these currents showing that they are mediated by NMDA receptors (Fig. 5*C*–*E*). In experiments where AP5 was bath applied before ZiMo12.8, AP5 occluded the effect of ZiMo12.8 on tonic currents (Fig. 5*F*,*G*), confirming that the inhibition of tonic currents by ZiMo12.8 depends on the function of NMDA receptors. Importantly, these effects of ZiMo12.8 were also observed when current density was used as the measurement of tonic NMDA receptor activity (Lu et al., 2006; Gall and Dupont, 2019; Wu et al., 2021; Wyroślak et al., 2023) suggesting that the effects are due to zinc inhibition of NMDAR and not due to changes in the cell capacitance in response to ZiMo12.8. We next hypothesized that if the effects of ZiMo12.8 result from ZIP12 antagonism, a different small molecule with low binding affinity for ZIP12 would not increase zinc-dependent inhibition of NMDA receptors. We therefore performed similar experiments with ZiMo12.9—which had no effect on HEK293 cell ZIP12-dependent zinc transport (Fig. 3*D*,*E*) and had low binding affinity for ZIP12 (Fig. 3*H*). Consistent with our hypothesis, ZiMo12.9 had no effect on tonic NMDA receptor currents in neurons (Fig. 5*H*,*I*). This result indicates that the inhibition of tonic NMDA receptor currents by ZiMo12.8 is not a general effect of small molecules, the vehicle used to deliver it into the ACSF, or due to other factors such as the duration of the whole-cell recordings or the dialysis of neuronal intracellular milieu that occurs in these experiments. Taken together, these electrophysiological results suggest that ZiMo12.8 acts to increase levels of synaptically released zinc in the extracellular space via decreasing the zinc transport activity of ZIP12 in the brain.

Discussion

As the importance of synaptic zinc in normal brain function is becoming more evident, there is a crucial need to understand

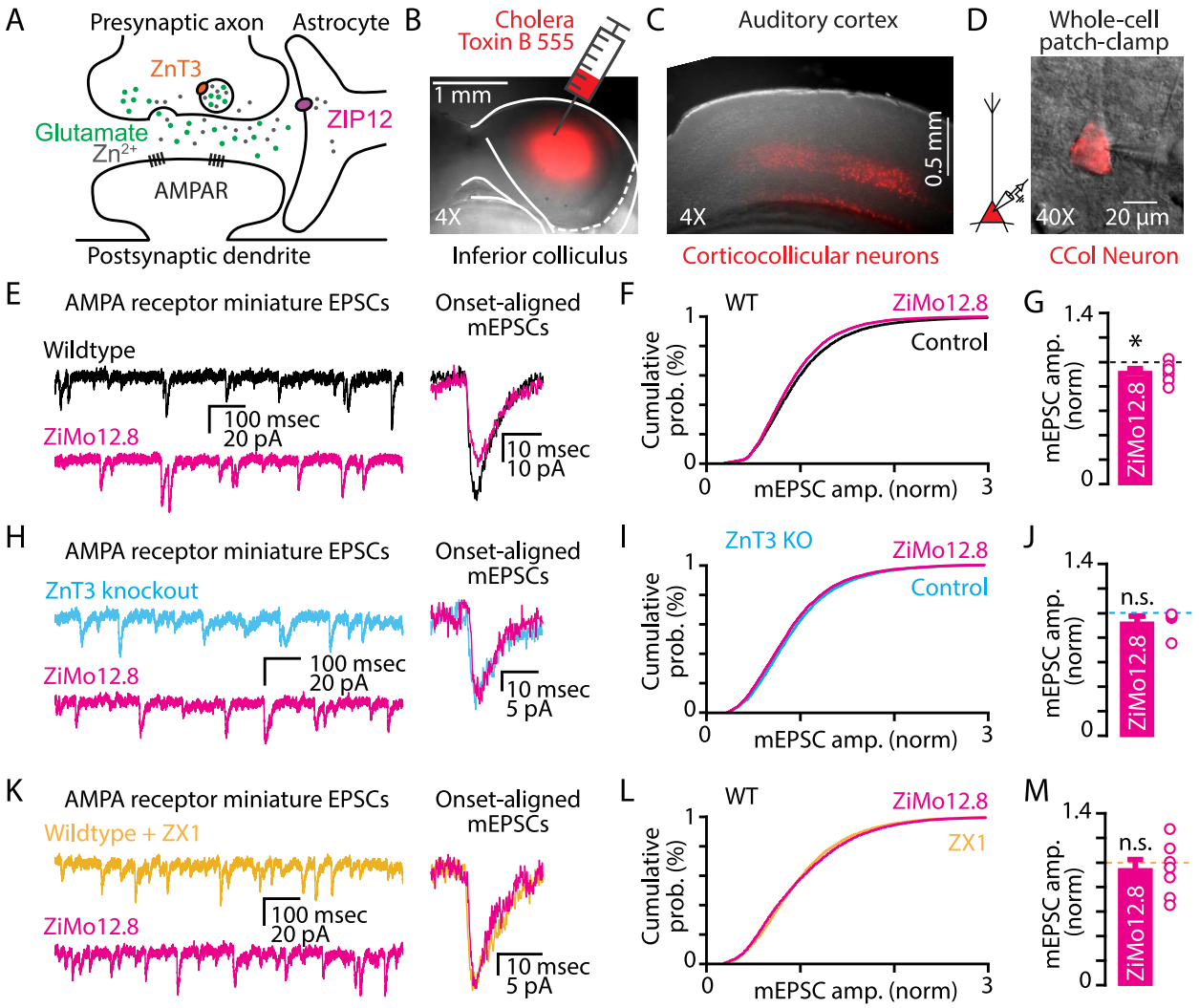

Figure 4. ZiMo12.8 increases ZnT3-dependent zinc inhibition of AMPA receptors in mouse ACx. ***A***, Cartoon of a tripartite glutamatergic synapse showing the corelease of zinc and glutamate into the synaptic cleft from the presynaptic neuron, where it acts on AMPA glutamate receptors of the postsynaptic neuron, with an astrocyte expressing ZIP12 clearing zinc from the cleft. ***B***, Example image of an acute brain slice of the inferior colliculus and schematic representation of the injection of the retrograde label cholera toxin subunit B conjugated to an Alexa Fluor 555 fluorophore (CTB-555). ***C***, Example image of an acute brain slice of ACx showing CTB-555 labeled corticocollicular (CCol) neurons in Layer 5. ***D***, Left, Schematic representation of a labeled CCol neuron in patch-clamp configuration. Right, Example image of a labeled CCol neuron in the ACx in whole-cell patch–clamp configuration. ***E***, Left, Example whole-cell patch–clamp recording of AMPA-mediated mEPSCs in acute brain slices of ACx from WT mice in both control conditions (black) and after bath application of ZiMo12.8 (pink). Right, Onset-aligned example mEPSCs from both before (black) and after (pink) treatment with ZiMo12.8. ***F***, Cumulative probability distribution showing AMPA-mediated mEPSC amplitudes normalized to the average amplitude of control mEPSCs in control conditions and after application of ZiMo12.8 in acute brain slices of ACx from WT mice. Colors as in ***E***. ***G***, Bar plot showing the average change in mEPSC amplitude after application of ZiMo12.8, normalized to the average amplitude of control mEPSCs in acute brain slices of ACx from WT mice (WT ZiMo12.8, mean = 0.925 ± 0.0295 SEM; $p = 0.0448$; $n = 7$ cells from 5 mice; paired t test). ***H***, Left, Example whole-cell patch–clamp recording of AMPA-mediated mEPSCs in acute brain slices of ACx from ZnT3 KO mice in both control conditions (blue) and after bath application of the novel ZIP12 antagonist ZiMo12.8 (pink). (Right) Onset-aligned example mEPSCs from both before (blue) and after (pink) application of ZiMo12.8. ***I***, Cumulative probability distribution showing the cumulative probability of AMPA-mediated mEPSC amplitudes normalized to the average amplitude of control mEPSCs in control conditions and after application of ZiMo12.8 in acute brain slices of ACx from ZnT3 KO mice. Colors as in ***H***. ***J***, Bar plot showing the average change in mEPSC amplitude after application of ZiMo12.8, normalized to the average amplitude of control mEPSCs in acute brain slices of ACx from ZnT3 KO mice (ZnT3 KO ZiMo12.8, mean = 0.919 ± 0.05557 SEM; $p = 0.2453$; $n = 7$ cells from 5 mice; paired t test). ***K***, Left, Example whole-cell patch–clamp recording of AMPA-mediated mEPSCs in acute brain slices of ACx from WT mice pretreated with ZX1 (yellow) and after bath application of ZiMo12.8 (pink). Right, Onset-aligned example mEPSCs from both before (yellow) and after (pink) treatment with ZiMo12.8. ***L***, Cumulative probability distribution showing the cumulative probability of AMPA-mediated mEPSC amplitudes normalized to the average amplitude of control mEPSCs in control conditions and after application of ZiMo12.8 in acute brain slices of ACx from WT mice pretreated with ZX1. Colors as in ***K***. ***M***, Bar plot showing the average change in mEPSC amplitude after application of ZiMo12.8, normalized to the average amplitude of control mEPSCs in acute brain slices of ACx from WT mice pretreated with ZX1 (WT with ZX1 + ZiMo12.8, mean = 0.941 ± 0.0826 SEM; $p = 0.4982$; $n = 4$ cells from 3 mice; paired t test). Asterisks (*) indicate statistically significant values. All values are given as mean ± SEM.

the cellular and molecular mechanisms that control the dynamics of this powerful signaling system. This need is made more urgent because of the growing body of evidence that links altered synaptic zinc signaling to neurological conditions such as autism (Yoo et al., 2016), schizophrenia (Carrera et al., 2012; Perez-Becerril et al., 2016), and Alzheimer's disease (Lee et al., 2002; Beyer et al., 2009; Adlard et al., 2010) suggesting that synaptic zinc signaling could provide novel targets for therapeutic approaches in the treatment of these disorders. While the importance of ZnT3 for loading zinc ions into synaptic vesicles is well established (Palmiter et al., 1996; Kantheti et al., 1998; Cole et al., 1999; 2001; Vogt et al., 2000; Salazar et al., 2005, 2009; Upmanyu

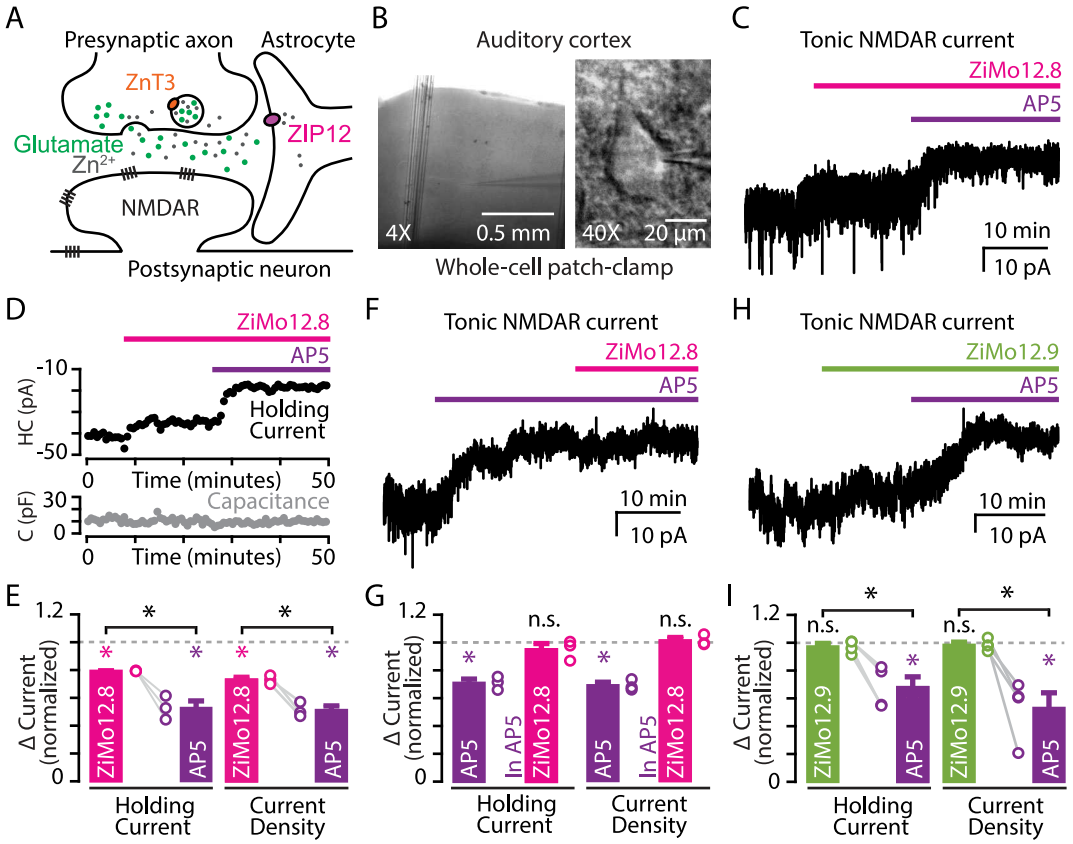

Figure 5. ZiMo12.8 increases ZnT3-dependent zinc inhibition of NMDA receptors in mouse ACx. ***A***, Cartoon of a tripartite glutamatergic synapse showing the corelease of zinc and glutamate into the synaptic cleft from the presynaptic neuron, where it acts on NMDA glutamate receptors of the postsynaptic neuron, with an astrocyte expressing ZIP12 clearing zinc from the cleft. ***B***, Left, Schematic representation of a layer 5 cortical neuron in patch-clamp configuration. Right, Example image of a layer 5 cortical neuron in the ACx in whole-cell patch–clamp configuration. ***C***, Left, Example patch-clamp recording of the tonic NMDA receptor current from a layer 5 neuron in an acute brain slice of the ACx from WT mice, with the application of ZiMo12.8 (pink) and the NMDAR antagonist AP5 (purple). ***D***, Top, Time course of tonic current recorded from the same cell in ***C***, with the application of ZiMo12.8 (pink) and the NMDAR antagonist AP5 (purple). Bottom, Corresponding time course of capacitance measurements for the same cell. ***E***, Bar plot showing the change in holding current (left) and current density (right) after the application of ZiMo12.8 and AP5 (holding current, ZiMo12.8, mean = 0.791 ± 0.00129 SEM; $p = 3.82 \times 10^{-5}$; AP5, mean = 0.527 ± 0.0492 SEM; $p = 0.0107$; ZiMo12.8 vs AP5, $p = 0.034$; current density, ZiMo12.8, mean = 0.7372 ± 0.017889 SEM; $p = 0.0046$; AP5, mean = 0.51641 ± 0.0308 SEM; $p = 0.0040$; ZiMo12.8 vs AP5, $p = 0.0204$; $n = 3$ cells from 3 mice; paired *t* test). Colors as in ***D***. ***F***, Example patch-clamp recording of the tonic NMDA current from a layer 5 neuron in an acute brain slice of the ACx from WT mice, with the application of the NMDAR antagonist AP5 (purple) before application of ZiMo12.8 (pink). ***G***, Bar plot showing the change in holding current (left) and current density (right) as a measure of tonic NMDA in control conditions and after the application of AP5 and after the application of ZiMo12.8 in AP5 (holding current, WT + AP5, mean = 0.71208 ± 0.027692 SEM; $p = 0.0091$; AP5 + ZiMo12.8, mean = 0.9474 ± 0.041436 SEM; $p = 0.3392$; current density, WT + AP5, mean = 0.68877 ± 0.022718; $p = 0.0053$; AP5 + ZiMo12.8, mean = 1.0112 ± 0.022636 SEM; $p = 0.6688$; $n = 3$ cells from 3 mice; paired *t* test.) Colors as in ***D***. ***H***, Example patch-clamp recording of the tonic NMDA current from a layer 5 neuron in an acute brain slice of the ACx from WT mice, with the application of the ZiMo12.9 (green) and the NMDAR antagonist AP5 (purple). ***I***, Bar plot showing the change in holding current (left) and current density (right) as a measure of tonic NMDA in control conditions, and after the application of ZiMo12.9 and AP5 (holding current, WT + ZiMo12.9, mean = 0.96886 ± 0.022698 SEM; $p = 0.2637$; WT + AP5, mean = 0.67735 ± 0.074598 SEM; $p = 0.0228$; WT + ZiMo12.9 vs WT + AP5, $p = 0.0132$; current density, WT + ZiMo12.9, mean = 1.009 ± 0.020602 SEM; $p = 0.6910$; WT + AP5, mean = 0.54374 ± 0.11247 SEM; $p = 0.0270$; WT + ZiMo12.9 vs WT + AP5, $p = 0.0262$; $n = 4$ cells from 4 mice; paired *t* test). Colors as in ***H***, Asterisks (*) indicate statistically significant values. All values are given as mean ± SEM.

et al., 2022), much less is known about the molecular machinery that controls synaptic zinc levels during synaptic transmission. Here we identify ZIP12 as a protein that contributes to extracellular zinc levels during synaptic transmission.

Synaptic zinc as a potent neuromodulatory signaling system (Pan et al., 2011; Vergnano et al., 2014; Anderson et al., 2015; Kalappa et al., 2015; Kouvaros et al., 2020; Cody and Tzounopoulos, 2022) that supports normal sensory processing (Anderson et al., 2017; Wu and Dyck, 2018; Kumar et al., 2019; Bender et al., 2023; McCollum et al., 2024) and ZnT3 KO mice (which lack synaptic zinc) display a range of cognitive, sensory, and behavioral deficits (Adlard et al., 2010; Martel et al., 2011; Sindreu et al., 2011; Yoo et al., 2016; Thackray et al., 2017; Wu and Dyck, 2018; Kumar et al., 2019; Zong et al., 2024). Synaptic zinc affects multiple aspects of excitatory and inhibitory neurotransmission. Exogenous zinc is an allosteric modulator that inhibits NMDA receptors (Legendre and Westbrook, 1990), with GluN2A-containing NMDA receptors inhibited by nanomolar levels of zinc (Paoletti et al., 1997; Tovar and Westbrook, 2012; Hansen et al., 2014). More recent work demonstrates that endogenous, synaptically released zinc inhibits NMDA receptors and affects synaptic plasticity (Vogt et al., 2000; Pan et al., 2011; Vergnano et al., 2014; Anderson et al., 2015). Synaptic zinc inhibits or potentiates AMPA receptor function (Kalappa et al., 2015; Bender et al., 2023) and triggers endocannabinoid synthesis that acts as a retrograde messenger to reduce presynaptic vesicular release probability (Perez-Rosello et al., 2013) and regulates chloride gradients and GABA signaling (Chorin et al., 2011) via the actions of the metabotropic zinc receptor GPR39 (Hershfinkel, 2018). At different concentrations, zinc also allosterically inhibits GABA receptors (Barberis et al., 2000), inhibits or potentiates glycine receptor function

(Trombley et al., 2011; Perez-Rosello et al., 2015), and potentiates kainate glutamate receptors (Veran et al., 2012). Our results uncover additional synaptic mechanisms that can contribute to the time course and concentration of zinc during synaptic transmission, which are crucial for determining the physiologically relevant roles of zinc at specific synapses in the brain.

Our results add to the growing list of zinc transporter proteins that contribute to synaptic signaling in the brain. Recent work has clearly shown that ZnT1 associates with GluN2A-containing NMDA receptors and contributes to zinc inhibition of these glutamate receptors at synaptic connections in the central nervous system (Krall et al., 2020). In addition, ZIP4 expressed by neurons forms close associations with synaptic proteins in the dendrites of cultured neurons (De Benedictis et al., 2021). Thus, our findings that the astrocytic protein ZIP12 is also a synaptic protein increase the compliment of zinc transporter proteins that support synaptic physiology and synaptic zinc signaling. Together, these results extend the network of synaptic proteins in the brain that coordinate the effects of synaptic zinc on synaptic transmission and further expand the repertoire of astrocytic proteins that support synaptic function.

In this study, we have identified ZIP12 as a synaptic protein and targeted its function at mouse cortical synapses. Pharmacological agents to selectively interfere with the removal of neurotransmitters from the synaptic cleft are powerful tools used for investigating synaptic function. From acetylcholinesterase inhibitors (Colović et al., 2013), glutamate reuptake inhibitors (Shimamoto et al., 1998), and GABA reuptake inhibitors (Braestrup et al., 1990), advancements in our understanding of synaptic physiology based on these tools have contributed to our understanding of synaptic function. This study identifies another synaptic protein to target with pharmacological agents to affect brain function. The zinc transporter system is an appealing target for neuromodulation because of its synapse specificity (Zeisel et al., 2015; Yao et al., 2021; Bender et al., 2023). Since not all synapses contain ZnT3 (Manning et al., 2024) or the same number or composition of AMPA and NMDA receptors (Nusser et al., 1998; Nusser, 2000; Masugi-Tokita et al., 2007), it is likely that zinc can have a diverse range of effects based on synapse-specific zinc release and clearance and on the specific expression of glutamate receptors. Unlike agents that target NMDA receptors such as ketamine and memantine (Johnson et al., 2015; Zhang et al., 2021; Chou et al., 2022; Wilcox et al., 2022; Ma et al., 2023) which are widely expressed throughout the nervous system, ZIP12 modulators have the potential to selectively affect glutamate receptors at synapses that express both ZnT3 and ZIP12, offering the ability to more precisely target certain synapses in the brain. Future studies establishing the specificity and potency of pharmacological compounds for ZIP12 over other zinc transporters (such as ZIP4; Kambe et al., 2015) will be required to more fully interpret the effects of ZIP12 antagonists on synaptic signaling and brain function. Our present results show that the effects of ZiMo12.8 depend on the presence of ZIP12, ZnT3, extracellular zinc, and glutamate receptors, but do not rule out possible effects of ZiMo12.8 on other protein targets. The lack of effect of ZiMo12.8 on zinc levels in native HEK293 cells suggests that this compound has specific actions on ZIP12; however, future experiments to characterize the potency and specificity of ZiMo12.8 for ZIP12 will be required to understand and address potential off-target interactions of ZiMo12.8 with other proteins.

Astrocytes are integral components of synapses throughout the brain (Eroglu and Barres, 2010; Khakh and Sofroniew, 2015; Khakh and Deneen, 2019). They tile cortical space so that a single astrocyte supports the function of many types of synapses that occur within each astrocyte's spatial domain (Bushong et al., 2002, 2004; Baldwin et al., 2024). Astrocytes are sensitive to neurotransmitters such as GABA, acetylcholine, and adenosine triphosphate (Durkee and Araque, 2019) and can express neurotransmitter receptors such as muscarinic acetylcholine receptors, dopamine receptors, metabotropic GABA receptors, and purinergic receptors (Shan et al., 2021). Because they are also sensitive to glutamate via the actions of EAAT1 and EAAT2 (Chaudhry et al., 1995; Bergles et al., 1997; Diamond et al., 1998; Petr et al., 2015; Sipe et al., 2021) and metabotropic glutamate receptors (Panatier et al., 2011; Morel et al., 2014), they have simultaneous access to multiple modes of synaptic signaling that occur within their territory. Combined with their ability to generate intracellular calcium transients (Goenaga et al., 2023; Gau et al., 2024) that can propagate to neighboring astrocytes (Kuga et al., 2011; Fujii et al., 2017), there is an emerging appreciation for a signaling role of astrocytes in information processing (Papouin et al., 2017) and synaptic development (Sipe et al., 2021) and as additional pathways for information propagation in the brain (Araque et al., 2014). Together, our findings highlight another contribution of non-neuronal brain cells to synaptic function, further expanding the repertoire of how these cells can contribute to normal and pathological conditions relating to zinc signaling in the brain.

Limitations

In this study we report the role of the astrocytic zinc transporter protein ZIP12 to contribute to synaptic function, identify pharmacological agents to target this protein, and use one of these agents to increase zinc levels in mouse brain slices. However, while our current results cannot rule out effects of ZiMo12.8 on other proteins, the effects of ZiMo12.8 on glutamate receptors depend on ZnT3-dependent zinc. Future experiments designed to increase the specificity and potency of small molecules for ZIP12 compared with other proteins and zinc transporters, such as ZIP4, will be required to fully characterize these tools. Additionally, more refined heterologous expression systems (such as astrocyte cultures) in combination with genetic deletion or silencing approaches in the brain to knock out or knock down ZIP12 in specific cell types will be required to more fully understand the specific roles of this zinc transporter in the brain. Overall, this study establishes ZIP12 as a synaptic protein that supports synaptic function, reveals molecular pathways important for brain function, and suggests potential targets for therapeutic interventions based on modulating zinc's effects on synaptic physiology.

References

Adlard PA, Parncutt JM, Finkelstein DI, Bush AI (2010) Cognitive loss in zinc transporter-3 knock-out mice: a phenocopy for the synaptic and memory deficits of Alzheimer's disease? J Neurosci 30:1631–1636.

Adlard PA, Parncutt J, Lal V, James S, Hare D, Doble P, Finkelstein DI, Bush AI (2015) Metal chaperones prevent zinc-mediated cognitive decline. Neurobiol Dis 81:196–202.

Adlard PA, Sedjahtera A, Gunawan L, Bray L, Hare D, Lear J, Doble P, Bush AI, Finkelstein DI, Cherny RA (2014) A novel approach to rapidly prevent age-related cognitive decline. Aging Cell 13:351–359.

Anderson CT, Kumar M, Xiong S, Tzounopoulos T (2017) Cell-specific gain modulation by synaptically released zinc in cortical circuits of audition. eLife 6:e29893.

Anderson CT, Radford RJ, Zastrow ML, Zhang DY, Apfel UP, Lippard SJ, Tzounopoulos T (2015) Modulation of extrasynaptic NMDA receptors by synaptic and tonic zinc. Proc Natl Acad Sci U S A 112:E2705–14.

Araque A, Carmignoto G, Haydon PG, Oliet SH, Robitaille R, Volterra A (2014) Gliotransmitters travel in time and space. Neuron 81:728–739.
Ashkenazy H, Abadi S, Martz E, Chay O, Mayrose I, Pupko T, Ben-Tal N (2016) Consurf 2016: an improved methodology to estimate and visualize evolutionary conservation in macromolecules. Nucleic acids research 44: W344–W350.
Baldwin KT, Murai KK, Khakh BS (2024) Astrocyte morphology. Trends Cell Biol 34:547–565.
Barberis A, Cherubini E, Mozrzymas JW (2000) Zinc inhibits miniature GABAergic currents by allosteric modulation of GABAA receptor gating. J Neurosci 20:8618–8627.
Bender PTR, McCollum M, Boyd-Pratt H, Mendelson BZ, Anderson CT (2023) Synaptic zinc potentiates AMPA receptor function in mouse auditory cortex. Cell Rep 42:112932.
Bergles DE, Dzubay JA, Jahr CE (1997) Glutamate transporter currents in Bergmann glial cells follow the time course of extrasynaptic glutamate. Proc Natl Acad Sci U S A 94:14821–14825.
Beyer N, Coulson DT, Heggarty S, Ravid R, Irvine GB, Hellemans J, Johnston JA (2009) Znt3 mRNA levels are reduced in Alzheimer's disease post-mortem brain. Mol Neurodegener 4:53.
Bin BH, Fukada T, Hosaka T, Yamasaki S, Ohashi W, Hojyo S, Miyai T, Nishida K, Yokoyama S, Hirano T (2011) Biochemical characterization of human ZIP13 protein: a homo-dimerized zinc transporter involved in the spondylocheiro dysplastic Ehlers-Danlos syndrome. J Biol Chem 286:40255–40265.
Blakemore LJ, Trombley PQ (2004) Diverse modulation of olfactory bulb AMPA receptors by zinc. Neuroreport 15:919–923.
Blakemore LJ, Trombley PQ (2019) Mechanisms of zinc modulation of olfactory bulb AMPA receptors. Neuroscience 410:160–175.
Boisvert MM, Erikson GA, Shokhirev MN, Allen NJ (2018) The aging astrocyte transcriptome from multiple regions of the mouse brain. Cell Rep 22: 269–285.
Braestrup C, Nielsen EB, Sonnewald U, Knutsen LJ, Andersen KE, Jansen JA, Frederiksen K, Andersen PH, Mortensen A, Suzdak PD (1990) (R)-N-[4,4-bis(3-methyl-2-thienyl)but-3-en-1-yl]nipecotic acid binds with high affinity to the brain gamma-aminobutyric acid uptake carrier. J Neurochem 54:639–647.
Bunch L, Erichsen MN, Jensen AA (2009) Excitatory amino acid transporters as potential drug targets. Expert Opin Ther Targets 13:719–731.
Bushong EA, Martone ME, Ellisman MH (2004) Maturation of astrocyte morphology and the establishment of astrocyte domains during postnatal hippocampal development. Int J Dev Neurosci 22:73–86.
Bushong EA, Martone ME, Jones YZ, Ellisman MH (2002) Protoplasmic astrocytes in CA1 stratum radiatum occupy separate anatomical domains. J Neurosci 22:183–192.
Carrera N, et al. (2012) Association study of nonsynonymous single nucleotide polymorphisms in schizophrenia. Biol Psychiatry 71:169–177.
Chaudhry FA, Lehre KP, van Lookeren Campagne M, Ottersen OP, Danbolt NC, Storm-Mathisen J (1995) Glutamate transporters in glial plasma membranes: highly differentiated localizations revealed by quantitative ultrastructural immunocytochemistry. Neuron 15:711–720.
Chen X, Sun Y-C, Zhan H, Kebschull JM, Fischer S, Matho K, Huang ZJ, Gillis J, Zador AM (2019) High-throughput mapping of long-range neuronal projection using in situ sequencing. Cell 179:772–786.e19.
Chorin E, Vinograd O, Fleidervish I, Gilad D, Herrmann S, Sekler I, Aizenman E, Hershfinkel M (2011) Upregulation of KCC2 activity by zinc-mediated neurotransmission via the mZnR/GPR39 receptor. J Neurosci 31:12916–12926.
Chou TH, Epstein M, Michalski K, Fine E, Biggin PC, Furukawa H (2022) Structural insights into binding of therapeutic channel blockers in NMDA receptors. Nat Struct Mol Biol 29:507–518.
Chowanadisai W, Graham DM, Keen CL, Rucker RB, Messerli MA (2013) Neurulation and neurite extension require the zinc transporter ZIP12 (slc39a12). Proc Natl Acad Sci U S A 110:9903–9908.
Clarke LE, Liddelow SA, Chakraborty C, Münch AE, Heiman M, Barres BA (2018) Normal aging induces A1-like astrocyte reactivity. Proc Natl Acad Sci U S A 115:E1896–E1905.
Cody PA, Tzounopoulos T (2022) Neuromodulatory mechanisms underlying contrast gain control in mouse auditory cortex. J Neurosci 42:5564–5579.
Cole TB, Martyanova A, Palmiter RD (2001) Removing zinc from synaptic vesicles does not impair spatial learning, memory, or sensorimotor functions in the mouse. Brain Res 891:253–265.
Cole TB, Wenzel HJ, Kafer KE, Schwartzkroin PA, Palmiter RD (1999) Elimination of zinc from synaptic vesicles in the intact mouse brain by disruption of the ZnT3 gene. Proc Natl Acad Sci U S A 96:1716–1721.
Colović MB, Krstić DZ, Lazarević-Pašti TD, Bondžić AM, Vasić VM (2013) Acetylcholinesterase inhibitors: pharmacology and toxicology. Curr Neuropharmacol 11:315–335.
Dean B, Hopper S, Scarr E (2024) Changes in levels of the zinc transporter SLC39A12 in Brodmann's area 44: effects of sex, suicide, CNS pH and schizophrenia. J Psychiatr Res 177:177–184.
De Benedictis CA, Haffke C, Hagmeyer S, Sauer AK, Grabrucker AM (2021) Expression analysis of zinc transporters in nervous tissue cells reveals neuronal and synaptic localization of ZIP4. Int J Mol Sci 22:4511.
Diamond JS, Bergles DE, Jahr CE (1998) Glutamate release monitored with astrocyte transporter currents during LTP. Neuron 21:425–433.
Durkee CA, Araque A (2019) Diversity and specificity of astrocyte-neuron communication. Neuroscience 396:73–78.
Eberhardt J, Santos-Martins D, Tillack AF, Forli S (2021) AutoDock Vina 1.2.0: new docking methods, expanded force field, and python bindings. J Chem Inf Model 61:3891–3898.
Eroglu C, Barres BA (2010) Regulation of synaptic connectivity by glia. Nature 468:223–231.
Frederickson CJ, Koh J-YY, Bush AI (2005) The neurobiology of zinc in health and disease. Nat Rev Neurosci 6:449–462.
Fujii Y, Maekawa S, Morita M (2017) Astrocyte calcium waves propagate proximally by gap junction and distally by extracellular diffusion of ATP released from volume-regulated anion channels. Sci Rep 7:13115.
Gall D, Dupont G (2019) Tonic activation of extrasynaptic NMDA receptors decreases intrinsic excitability and promotes bistability in a model of neuronal activity. Int J Mol Sci 21:206.
Gau YA, Hsu ET, Cha RJ, Pak RW, Looger LL, Kang JU, Bergles DE (2024) Multicore fiber optic imaging reveals that astrocyte calcium activity in the mouse cerebral cortex is modulated by internal motivational state. Nat Commun 15:3039.
Goenaga J, Araque A, Kofuji P, Herrera Moro Chao D (2023) Calcium signaling in astrocytes and gliotransmitter release. Front Synaptic Neurosci 15: 1138577.
Hansen KB, Ogden KK, Yuan H, Traynelis SF (2014) Distinct functional and pharmacological properties of Triheteromeric GluN1/GluN2A/GluN2B NMDA receptors. Neuron 81:1084–1096.
Hershfinkel M (2018) The zinc sensing receptor, ZnR/GPR39, in health and disease. Int J Mol Sci 19:439.
Hoch E, Levy M, Hershfinkel M, Sekler I (2020) Elucidating the H^+ coupled Zn^{2+} transport mechanism of ZIP4; implications in acrodermatitis enteropathica. Int J Mol Sci 21:734.
Hruska M, Cain RE, Dalva MB (2022) Nanoscale rules governing the organization of glutamate receptors in spine synapses are subunit specific. Nat Commun 13:920.
Huang Z, Zhang XA, Bosch M, Smith SJ, Lippard SJ (2013) Tris(2-pyridylmethyl)amine (TPA) as a membrane-permeable chelator for interception of biological mobile zinc. Metallomics 5:648–655.
Icha J, Weber M, Waters JC, Norden C (2017) Phototoxicity in live fluorescence microscopy, and how to avoid it. Bioessays 39.
Insel TR (2010) Rethinking schizophrenia. Nature 468:187.
Johnson JW, Glasgow NG, Povysheva NV (2015) Recent insights into the mode of action of memantine and ketamine. Curr Opin Pharmacol 20:54–63.
Kalappa BI, Anderson CT, Goldberg JM, Lippard SJ, Tzounopoulos T (2015) AMPA receptor inhibition by synaptically released zinc. Proc Natl Acad Sci U S A 112:15749–15754.
Kambe T, Tsuji T, Hashimoto A, Itsumura N (2015) The physiological, biochemical, and molecular roles of zinc transporters in zinc homeostasis and metabolism. Physiol Rev 95:749–784.
Kantheti P, Qiao X, Diaz ME, Peden AA, Meyer GE, Carskadon SL, Kapfhamer D, Sufalko D, Robinson MS, Noebels JL (1998) Mutation in AP-3 δ in the mocha mouse links endosomal transport to storage deficiency in platelets, melanosomes, and synaptic vesicles. Neuron 21: 111–122.
Khakh BS, Deneen B (2019) The emerging nature of astrocyte diversity. Annu Rev Neurosci 42:187–207.
Khakh BS, Sofroniew MV (2015) Diversity of astrocyte functions and phenotypes in neural circuits. Nat Neurosci 18:942–952.
Kouvaros S, Kumar M, Tzounopoulos T (2020) Synaptic zinc enhances inhibition mediated by somatostatin, but not parvalbumin, cells in mouse auditory cortex. Cereb Cortex 30:3895–3909.

Krall RF, Moutal A, Phillips MB, Asraf H, Johnson JW, Khanna R, Hershfinkel M, Aizenman E, Tzounopoulos T (2020) Synaptic zinc inhibition of NMDA receptors depends on the association of GluN2A with the zinc transporter ZnT1. Sci Adv 6:eabb1515.

Kuga N, Sasaki T, Takahara Y, Matsuki N, Ikegaya Y (2011) Large-scale calcium waves traveling through astrocytic networks in vivo. J Neurosci 31: 2607–2614.

Kumar M, Xiong S, Tzounopoulos T, Anderson CT (2019) Fine control of sound frequency tuning and frequency discrimination acuity by synaptic zinc signaling in mouse auditory cortex. J Neurosci 39:854–865.

Lee JY, Cole TB, Palmiter RD, Suh SW, Koh JY (2002) Contribution by synaptic zinc to the gender-disparate plaque formation in human Swedish mutant APP transgenic mice. Proc Natl Acad Sci U S A 99:7705–7710.

Legendre P, Westbrook GL (1990) The inhibition of single N-methyl-D-aspartate-activated channels by zinc ions on cultured rat neurones. J Physiol 429:429–449.

Lu C, Fu Z, Karavanov I, Yasuda RP, Wolfe BB, Buonanno A, Vicini S (2006) NMDA receptor subtypes at autaptic synapses of cerebellar granule neurons. J Neurophysiol 96:2282–2294.

Ma S, et al. (2023) Sustained antidepressant effect of ketamine through NMDAR trapping in the LHb. Nature 622:802–809.

Magupalli VG, Schwarz K, Alpadi K, Natarajan S, Seigel GM, Schmitz F (2008) Multiple RIBEYE–RIBEYE interactions create a dynamic scaffold for the formation of synaptic ribbons. J Neurosci 28:7954–7967.

Manning A, Bender PTR, Boyd-Pratt H, Mendelson BZ, Hruska M, Anderson CT (2024) Trans-synaptic association of vesicular zinc transporter 3 and shank3 supports synapse-specific dendritic spine structure and function in the mouse auditory cortex. J Neurosci 44:e0619242024.

Martel G, Hevi C, Kane-Goldsmith N, Shumyatsky GP (2011) Zinc transporter ZnT3 is involved in memory dependent on the hippocampus and perirhinal cortex. Behav Brain Res 223:233–238.

Masugi-Tokita M, Tarusawa E, Watanabe M, Molnár E, Fujimoto K, Shigemoto R (2007) Number and density of AMPA receptors in individual synapses in the rat cerebellum as revealed by SDS-digested freeze-fracture replica labeling. J Neurosci 27:2135–2144.

Mayer ML, Westbrook GL, Guthrie PB (1984) Voltage-dependent block by Mg2+ of NMDA responses in spinal cord neurones. Nature 309:261–263.

McAllister BB, Dyck RH (2017a) Sound processing: a new role for zinc in the brain. eLife 6:e31816.

McAllister BB, Dyck RH (2017b) Zinc transporter 3 (ZnT3) and vesicular zinc in central nervous system function. Neurosci Biobehav Rev 80:329–350.

McCollum M, Manning A, Bender PTR, Mendelson BZ, Anderson CT (2024) Cell-type-specific enhancement of deviance detection by synaptic zinc in the mouse auditory cortex. Proc Natl Acad Sci U S A 121:e2405615121.

Morabito A, Zerlaut Y, Serraz B, Sala R, Paoletti P, Rebola N (2022) Activity-dependent modulation of NMDA receptors by endogenous zinc shapes dendritic function in cortical neurons. Cell Rep 38:110415.

Morel L, Higashimori H, Tolman M, Yang Y (2014) VGluT1+ neuronal glutamatergic signaling regulates postnatal developmental maturation of cortical protoplasmic astroglia. J Neurosci 34:10950–10962.

Nishikawa M, Mori H, Hara M (2017) Analysis of ZIP (Zrt-, Irt-related protein) transporter gene expression in murine neural stem/progenitor cells. Environ Toxicol Pharmacol 53:81–88.

Nusser Z (2000) AMPA and NMDA receptors: similarities and differences in their synaptic distribution. Curr Opin Neurobiol 10:337–341.

Nusser Z, Lujan R, Laube G, Roberts JD, Molnar E, Somogyi P (1998) Cell type and pathway dependence of synaptic AMPA receptor number and variability in the hippocampus. Neuron 21:545–559.

Ohana E, Hoch E, Keasar C, Kambe T, Yifrach O, Hershfinkel M, Sekler I (2009) Identification of the Zn2+ binding site and mode of operation of a mammalian Zn2+ transporter. J Biol Chem 284:17677–17686.

Palmiter RD, Cole TB, Quaife CJ, Findley SD (1996) ZnT-3, a putative transporter of zinc into synaptic vesicles. Proc Natl Acad Sci U S A 93:14934–14939.

Pan E, Zhang XA, Huang Z, Krezel A, Zhao M, Tinberg CE, Lippard SJ, McNamara JO (2011) Vesicular zinc promotes presynaptic and inhibits postsynaptic long-term potentiation of mossy fiber-CA3 synapse. Neuron 71:1116–1126.

Panatier A, Vallée J, Haber M, Murai KK, Lacaille JC, Robitaille R (2011) Astrocytes are endogenous regulators of basal transmission at central synapses. Cell 146:785–798.

Paoletti P, Ascher P, Neyton J (1997) High-affinity zinc inhibition of NMDA NR1-NR2A receptors. J Neurosci 17:5711–5725.

Papouin T, Dunphy J, Tolman M, Foley JC, Haydon PG (2017) Astrocytic control of synaptic function. Philos Trans R Soc Lond B Biol Sci 372:20160154.

Perea G, Navarrete M, Araque A (2009) Tripartite synapses: astrocytes process and control synaptic information. Trends Neurosci 32:421–431.

Perez-Becerril C, Morris AG, Mortimer A, McKenna PJ, de Belleroche J (2016) Common variants in the chromosome 2p23 region containing the SLC30A3 (ZnT3) gene are associated with schizophrenia in female but not male individuals in a large collection of European samples. Psychiatry Res 246:335–340.

Perez-Rosello T, Anderson CT, Ling C, Lippard SJ, Tzounopoulos T (2015) Tonic zinc inhibits spontaneous firing in dorsal cochlear nucleus principal neurons by enhancing glycinergic neurotransmission. Neurobiology of disease 81:14–19.

Perez-Rosello T, Anderson CT, Schopfer FJ, Zhao Y, Gilad D, Salvatore SR, Freeman BA, Hershfinkel M, Aizenman E, Tzounopoulos T (2013) Synaptic Zn2+ inhibits neurotransmitter release by promoting endocannabinoid synthesis. J Neurosci 33:9259–9272.

Petr GT, et al. (2015) Conditional deletion of the glutamate transporter GLT-1 reveals that astrocytic GLT-1 protects against fatal epilepsy while neuronal GLT-1 contributes significantly to glutamate uptake into synaptosomes. J Neurosci 35:5187–5201.

Povysheva NV, Johnson JW (2012) Tonic NMDA receptor-mediated current in prefrontal cortical pyramidal cells and fast-spiking interneurons. J Neurophysiol 107:2232–2243.

Rachline J, Perin-Dureau F, Le Goff A, Neyton J, Paoletti P (2005) The micromolar zinc-binding domain on the NMDA receptor subunit NR2B. J Neurosci 25:308–317.

Rose CR, Felix L, Zeug A, Dietrich D, Reiner A, Henneberger C (2018) Astroglial glutamate signaling and uptake in the hippocampus. Front Mol Neurosci 10:451.

Salazar G, Craige B, Love R, Kalman D, Faundez V (2005) Vglut1 and ZnT3 co-targeting mechanisms regulate vesicular zinc stores in PC12 cells. J Cell Sci 118:1911–1921.

Salazar G, Falcon-Perez JM, Harrison R, Faundez V (2009) SLC30A3 (ZnT3) oligomerization by dityrosine bonds regulates its subcellular localization and metal transport capacity. PLoS One 4:e5896.

Sander T, Freyss J, von Korff M, Rufener C (2015) DataWarrior: an open-source program for chemistry aware data visualization and analysis. J Chem Inf Model 55:460–473.

Scarr E, et al. (2016) Increased cortical expression of the zinc transporter SLC39A12 suggests a breakdown in zinc cellular homeostasis as part of the pathophysiology of schizophrenia. NPJ Schizophr 2:16002.

Schindelin J, et al. (2012) Fiji: an open-source platform for biological-image analysis. Nat Methods 9:676–682.

Seve M, Chimienti F, Devergnas S, Favier A (2004) In silico identification and expression of SLC30 family genes: an expressed sequence tag data mining strategy for the characterization of zinc transporters' tissue expression. BMC genomics 5:32.

Shan L, Zhang T, Fan K, Cai W, Liu H (2021) Astrocyte-neuron signaling in synaptogenesis. Front Cell Dev Biol 9:680301.

Shimamoto K, Lebrun B, Yasuda-Kamatani Y, Sakaitani M, Shigeri Y, Yumoto N, Nakajima T (1998) DL-threo-beta-benzyloxyaspartate, a potent blocker of excitatory amino acid transporters. Mol Pharmacol 53:195–201.

Sindreu C, Palmiter RD, Storm DR (2011) Zinc transporter ZnT-3 regulates presynaptic Erk1/2 signaling and hippocampus-dependent memory. Proc Natl Acad Sci U S A 108:3366–3370.

Sipe GO, Petravicz J, Rikhye RV, Garcia R, Mellios N, Sur M (2021) Astrocyte glutamate uptake coordinates experience-dependent, eye-specific refinement in developing visual cortex. Glia 69:1723–1735.

Styrpejko DJ, Cuajungco MP (2021) Transmembrane 163 (TMEM163) protein: a new member of the zinc efflux transporter family. Biomedicines 9: 220.

Surre J, Saint-Ruf C, Collin V, Orenga S, Ramjeet M, Matic I (2018) Strong increase in the autofluorescence of cells signals struggle for survival. Sci Rep 8:12088.

Suter BA, O'Connor T, Iyer V, Petreanu LT, Hooks BM, Kiritani T, Svoboda K, Shepherd GMG (2010) Ephus: multipurpose data acquisition software for neuroscience experiments. Front Neural Circuits 4:100.

Takao-Rikitsu E, Mochida S, Inoue E, Deguchi-Tawarada M, Inoue M, Ohtsuka T, Takai Y (2004) Physical and functional interaction of the active zone proteins, CAST, RIM1, and Bassoon, in neurotransmitter release. J Cell Biol 164:301–311.

Thackray SE, McAllister BB, Dyck RH (2017) Behavioral characterization of female zinc transporter 3 (ZnT3) knockout mice. Behav Brain Res 321:36–49.

tom Dieck S, Altrock WD, Kessels MM, Qualmann B, Regus H, Brauner D, Fejtová A, Bracko O, Gundelfinger ED, Brandstätter JH (2005) Molecular dissection of the photoreceptor ribbon synapse: physical interaction of bassoon and RIBEYE is essential for the assembly of the ribbon complex. J Cell Biol 168:825–836.

Tovar KR, Westbrook GL (2012) Amino-terminal ligands prolong NMDA receptor-mediated EPSCs. J Neurosci 32:8065–8073.

Trombley PQ, Blakemore LJ, Hill BJ (2011) Zinc modulation of glycine receptors. Neuroscience 186:32–38.

Trott O, Olson AJ (2010) AutoDock Vina: improving the speed and accuracy of docking with a new scoring function, efficient optimization, and multithreading. J Comput Chem 31:455–461.

Upmanyu N, et al. (2022) Colocalization of different neurotransmitter transporters on synaptic vesicles is sparse except for VGLUT1 and ZnT3. Neuron 110:1483–1497.e7.

Veran J, Kumar J, Pinheiro PS, Athané A, Mayer ML, Perrais D, Mulle C (2012) Zinc potentiates GluK3 glutamate receptor function by stabilizing the ligand binding domain dimer interface. Neuron 76:565–578.

Vergnano AM, Rebola N, Savtchenko LP, Pinheiro PS, Casado M, Kieffer BL, Rusakov DA, Mulle C, Paoletti P (2014) Zinc dynamics and action at excitatory synapses. Neuron 82:1101–1114.

Vogt K, Mellor J, Tong G, Nicoll R (2000) The actions of synaptically released zinc at hippocampal mossy fiber synapses. Neuron 26:187–196.

Wilcox MR, et al. (2022) Inhibition of NMDA receptors through a membrane-to-channel path. Nat Commun 13:4114.

Wu K, Castellano D, Tian Q, Lu W (2021) Distinct regulation of tonic GABAergic inhibition by NMDA receptor subtypes. Cell Rep 37:109960.

Wu HP, Dyck RH (2018) Signaling by synaptic zinc is required for whisker-mediated, fine texture discrimination. Neuroscience 369:242–247.

Wyroślak M, Dobrzański G, Mozrzymas JW (2023) Bidirectional plasticity of GABAergic tonic inhibition in hippocampal somatostatin- and parvalbumin-containing interneurons. Front Cell Neurosci 17:1193383.

Yao Z, et al. (2021) A taxonomy of transcriptomic cell types across the isocortex and hippocampal formation. Cell 184:3222–3241.e26.

Yariv B, Yariv E, Kessel A, Masrati G, Chorin AB, Martz E, Mayrose I, Pupko T, Ben-Tal N (2023) Using evolutionary data to make sense of macromolecules with a "face-lifted" ConSurf. Protein Science 32:e4582.

Yoo MH, Kim T-YY, Yoon YH, Koh J-YY (2016) Autism phenotypes in ZnT3 null mice: Involvement of zinc dyshomeostasis, MMP-9 activation and BDNF upregulation. Sci Rep 6:28548.

Zeisel A, Muñoz-Manchado AB, Codeluppi S, Lönnerberg P, La Manno G, Juréus A, Marques S, Munguba H, He L, Betsholtz C (2015) Cell types in the mouse cortex and hippocampus revealed by single-cell RNA-seq. Science 347:1138–1142.

Zhang Y, Chen K, Sloan SA, Bennett ML, Scholze AR, O'Keeffe S, Phatnani HP, Guarnieri P, Caneda C, Ruderisch N (2014a) An RNA-sequencing transcriptome and splicing database of glia, neurons, and vascular cells of the cerebral cortex. J Neurosci 34:11929–11947.

Zhang Y, Chen K, Sloan SA, Bennett ML, Scholze AR, O'Keeffe S, Phatnani HP, Guarnieri P, Caneda C, Ruderisch N (2014b) An RNA-sequencing transcriptome and splicing database of glia, neurons, and vascular cells of the cerebral cortex. J Neurosci 34:11929–11947.

Zhang T, Liu J, Fellner M, Zhang C, Sui D, Hu J (2017) Crystal structures of a ZIP zinc transporter reveal a binuclear metal center in the transport pathway. Science Advances 3:e1700344.

Zhang T, Sui D, Hu J (2016) Structural insights of ZIP4 extracellular domain critical for optimal zinc transport. Nat Commun 7:11979.

Zhang Y, Ye F, Zhang T, Lv S, Zhou L, Du D, Lin H, Guo F, Luo C, Zhu S (2021) Structural basis of ketamine action on human NMDA receptors. Nature 596:301–305.

Zong R, Zhang X, Dong X, Liu G, Zhang J, Gao Y, Zhang Z, Ma Y, Gao H, Gamper N (2024) Genetic deletion of zinc transporter ZnT_3 induces progressive cognitive deficits in mice by impairing dendritic spine plasticity and glucose metabolism. Front Mol Neurosci 17:1375925.